Evaluation of high strength steels fracture based on uniaxial stress-strain curves

Xin, Haohui; Veljkovic, Milan

DOI
10.1016/j.engfailanal.2020.105025

Publication date
2021

Document Version
Final published version

Published in
Engineering Failure Analysis

Citation (APA)
Xin, H., & Veljkovic, M. (2021). Evaluation of high strength steels fracture based on uniaxial stress-strain curves. *Engineering Failure Analysis*, *120*, 1-30. Article 105025. https://doi.org/10.1016/j.engfailanal.2020.105025

Engineering Failure Analysis 120 (2021) 105025

Contents lists available at ScienceDirect

Engineering Failure Analysis

journal homepage: www.elsevier.com/locate/engfailanal

Evaluation of high strength steels fracture based on uniaxial stress-strain curves

Haohui Xin [a,b,*], Milan Veljkovic [b]

[a] *Department of Civil Engineering, School of Human Settlements and Civil Engineering, Xi'an Jiaotong University, Xi'an, Shaanxi 710049, China*[1]
[b] *Faculty of Civil Engineering and Geosciences, Delft University of Technology, Netherlands*[2]

ARTICLE INFO

Keywords:
High strength steel (HSS)
Ductile fracture
Hosford-Coulomb fracture strain

ABSTRACT

Predicting the ultimate capacity of components made of high strength steel (HSS) is a numerically challenging task. The fracture performance of HSS from different steel grades, producers, and manufacturing processes (rolling, cold forming, etc.) varies greatly. It is costly to conduct a series of experiments for each typical HSS structural component to identify the parameters of the fracture model. An attempt is made to evaluate the fracture material properties based only on the standardized uniaxial stress-strain curve. The uncoupled fracture model was implemented through a user subroutine VUMAT (ABAQUS) to evaluate the ductile fracture of HSS, where a rate-independent non-linear isotropic J2 hardening model is used in combination with a separate Hosford-Coulomb fracture model. The detailed procedure to identify the material parameters based on only the uniaxial stress-strain curve of steel grades S700 and S960 are provided for the sake of illustration of possible applications. The proposed fracture model and identified parameters are validated based on the experimental results of the HSS plate with different hole sizes in the middle of the dog bone specimens. Besides, a desktop study of a single K gap joint with $\beta = 0.5$ made of square hollow sections using S700 and S960 is used to illustrate a possible application of the fracture model in a simplified model of the structural joint.

1. Introduction

The usage of high strength steel (HSS) structure is increasing because of its economical and functional advantages [1–6]. Evaluation of the ductile fracture of HSS components benefits the economical design. Predicting the bearing capacities of HSS components, such as hollow section joints for lager span truss girder, semi-grid beam-column bolted joints, etc., is very important.

The failure of HSS is a progressive material deterioration due to the nucleation, growth, and coalescence of micro-voids [7]. The fracture models of steels generally consist of physically based and phenomenological models. The physically-based model assumed that the fracture occurs when the micro void radius or void volume fraction reaches a critical threshold value. Early physically-based ductile fracture prediction is developed by analyzing the evolution of cylindrical and spherical holes in a ductile matrix by McClintock (1968) [8] and Rice & Tracey(1969) [9]. Gurson(1977) [10] proposed a (porous) plasticity model which includes the void volume fraction as an internal variable. The original Gurson model is improved to consider void coalescence by Tevergaard and Needleman

---

[*] Corresponding author.
E-mail address: H.Xin@tudelft.nl (H. Xin).
[1] Present.
[2] Previous.

https://doi.org/10.1016/j.engfailanal.2020.105025
Received 16 August 2020; Received in revised form 20 September 2020; Accepted 17 October 2020

(1984) [11,12], known as Gurson- Tevergaard-Needleman (GTN) model. The GTN model is further extended to consider anisotropy [13] and shear effects [14]. The phenomenological models, such as the Johnson-Cook model [15], MMC model [16], and Hosford-Coulomb model [17,18], assumed that fracture occurs at a point where a weighted measure of the accumulated equivalent plastic strain reaches a critical value. The research of Mohr&Marcadet (2015), Bai&Wierzbicki (2008 and 2004), and Lou et al (2014) [19–22] showed that the equivalent plastic strain at the onset of fracture is the function of the stress triaxiality and the Lode (angle) parameter. The constant request of reliable experimental data characterizing the effect stress status on ductile fracture is necessary to guarantee the accuracy of the phenomenological ductile models. The stress status is generally achieved through different initial specimen geometries or by applying different load combinations.

There is a big potential application in predicting the ductile fracture of critical components of HSS structures in the construction sector. However, the parameters of physically-based fracture model could not be identified conveniently [23], and the phenomenological models assume to conduct a series of experiments for each typical component to identify the parameters but the ductile performance of HSS from different steel grade, producers, manufacturing process (cold-formed, hot rolled, etc.) varies a lot. An example of differences of the nominally same steel grades S700 and S960 from different producers are shown in [24]. Thus, one of the common issues for HSS structures is to identify the parameters of the ductile fracture model conveniently from the uniaxial stress-strain obtained from common coupon specimens [25–27].

In this paper, an attempt is made to evaluate the ductile fracture of HSS based on phenomenological fracture models only from the uniaxial stress-strain curve. Uncoupled fracture model was implemented using a user subroutine VUMAT (ABAQUS) to evaluate the ductile fracture parameters of HSS, where a rate-independent non-linear isotropic J2 hardening model is used in combination with a separate Hosford-Coulomb fracture model. The detailed procedure to identify the material parameters based on the uniaxial stress-strain curve of HSS S700 and S960 is illustrated by FEA and experimental results. The proposed fracture model and identified parameters are successfully validated based on the experimental results of the HSS flat specimens with different hole sizes in the middle of the dog bone specimen. Fracture simulation is performed on an individual K gap joint made of square hollow sections as a case study.

2. Ductile fracture model

The ductile fracture model is divided into two parts in this paper, namely plasticity and ductile damage. For simplicity, a rate-independent non-linear isotropic J2 hardening model is used to describe the steel plasticity, and the Hosford-Coulomb model [17,18] is used to predict steel fracture. A user subroutine VUMAT [28] based on the commercial finite element (FE) software ABAQUS is implemented.

2.1. Plasticity model formulation

The rate-independent non-linear isotropic J2 hardening model is employed to define the steel plasticity [28]. The isotropic yield function is written in terms of the von Mises equivalent stress $\overline{\sigma}$ and the yield strength s:

$$f = \overline{\sigma} - s = 0 \tag{1}$$

The equivalent Mises stress is shown as below:

$$\overline{\sigma} = \sqrt{\frac{3}{2} S_{ij} S_{ij}} \tag{2}$$

where S_{ij} is the deviatoric stress tensor:

$$S_{ij} = \sigma_{ij} - \sigma_m \tag{3}$$

where σ_m is the mean stress:

$$\sigma_m = \frac{1}{3}\sigma_{ii} \tag{4}$$

The associated plastic flow rule, where the plastic strain increment and deviatoric stress tensor have the same principle direction, is given by:

$$\dot{\varepsilon}^p_{ij} = \dot{\lambda}\frac{\partial f}{\partial \sigma_{ij}} \tag{5}$$

where $\dot{\lambda}$ is a positive scalar factor.

2.2. Fracture model

Uncoupled fracture model was employed to describe the ductile fracture of metals [29], where standard plasticity models are used in combination with a separate fracture model. The basic assumption of the uncoupled model is that the evolution of damage does not affect the effective stress-strain response of HSS before a fracture occurs. The evolution of a scalar damage indicator is described

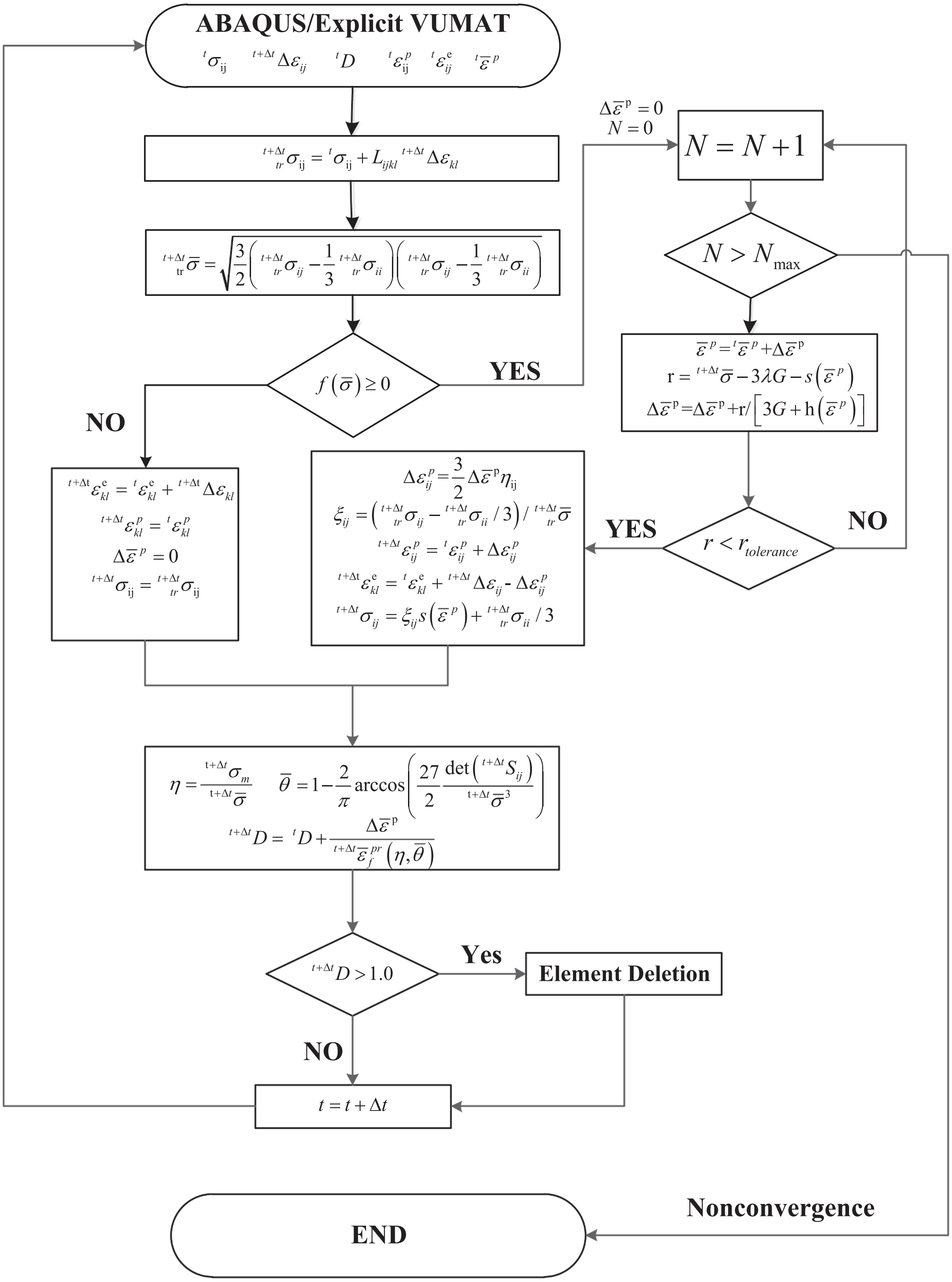

Fig. 1. Implementation flow chart of ductile fracture model.

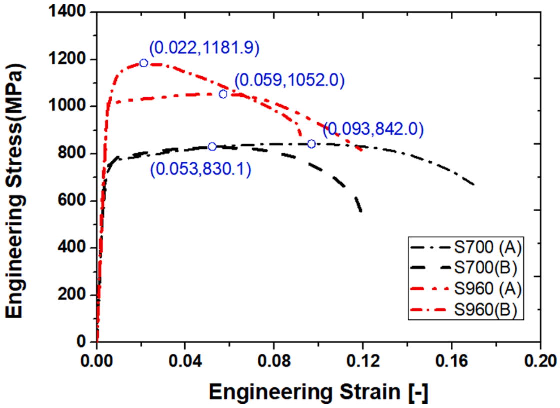

Fig. 2. Engineering strain vs. Engineering stress of HSS.

through integration, expressed in Eq. (6). D = 0 denoted no damage, D = 1 denoted the fracture.

$$D = \int_0^{\overline{\varepsilon}_p^f} \frac{d\overline{\varepsilon}_p}{\overline{\varepsilon}_f^{pr}(\eta, \overline{\theta})} \tag{6}$$

The equivalent plastic strain [17,18] $\overline{\varepsilon}_f^{pr}$ at the onset of fracture is the function of the stress triaxiality η and the Lode angle parameter $\overline{\theta}$, given by:

$$\overline{\varepsilon}_f^{pr}(\eta, \overline{\theta}) = b(1+c)^{1/n}\left(\left\{\frac{1}{2}\left[(f_1 - f_2)^a + (f_2 - f_3)^a + (f_1 - f_3)^a\right]\right\}^{1/a} + c(2\eta + f_1 + f_3)\right)^{-1/n} \tag{7}$$

Where: a is the Hosford exponent, that controls measurement of the deviatoric stress; b is the material parameter that controls the overall level of the fracture strains; and c is the friction coefficient in the Hosford-Coulomb model, that controls the influence of the normal stress; n is the transformation constant. The functions $f_i(i = 1, 2, 3)$ are Lode angle parameter-dependent functions, that are associated with the transformation from principal stresses to Haigh-Westergaard cylindrical coordinate system [17,18],

$$f_1[\overline{\theta}] = \frac{2}{3}cos\left[\frac{\pi}{6}(1 - \overline{\theta})\right] \tag{8}$$

$$f_2[\overline{\theta}] = \frac{2}{3}cos\left[\frac{\pi}{6}(3 + \overline{\theta})\right] \tag{9}$$

$$f_3[\overline{\theta}] = -\frac{2}{3}cos\left[\frac{\pi}{6}(1 + \overline{\theta})\right] \tag{10}$$

The stress triaxiality η is defined as the ratio between mean stress and von Mises stress, given by:

$$\eta = \frac{\sigma_m}{\overline{\sigma}} \tag{11}$$

The Lode angle parameter $\overline{\theta}$ is defined as [17,18]:

$$\overline{\theta} = 1 - \frac{2}{\pi}arccos\left(\frac{27}{2}\frac{J_3}{\overline{\sigma}^3}\right) \cong -\frac{2\sigma_2 - \sigma_1 - \sigma_3}{\sigma_1 - \sigma_3} \tag{12}$$

Where: $\sigma_i(i = 1, 2, 3)$ is the principal stress, J_3 is the third invariants of the Cauchy stress deviator, expressed as the determinant of the deviatoric stress tensor:

$$J_3 = det(S_{ij}) \tag{13}$$

2.3. Implementation

The ductile fracture model is implemented through user subroutine VUMAT [28] see Fig. 1.

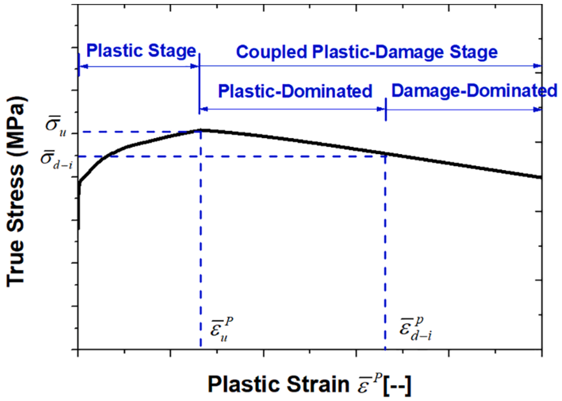

Fig. 3. Plastic and coupled plastic-damage stages (Necking and damage effects are not considering for true stress).

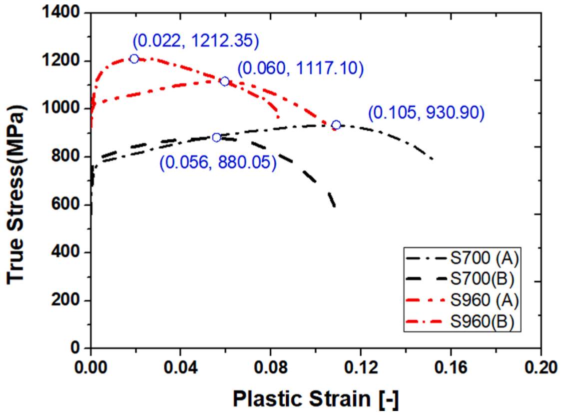

Fig. 4. True stress vs. plastic strain, no necking and damage effects.

3. Identification of ductile fracture parameters

To predict the ductile fracture of high strength steels, this paper divided the identification process into two stages: Identify the relationship between equivalent plastic strain and uniaxial true stress for the isotropic J2 plasticity model; ②Identify parameters of fracture strain under multiaxial stress states for Hosford-Coulomb fracture model. Explanation of the identification procedures is shown below for steel grades S700 and S960, from two different steel producers (company A and company B), see Fig. 2, obtained in the RUOSTE project [24].

3.1. Plasticity parameter identification

It is assumed that the evolution of damage does not affect the uniaxial true stress-strain response of HSS before a fracture occurs for the uncoupled fracture model [23]. The first task of parameter identification is to determine the relationship between uniaxial plastic strain and the true stress based on engineering strain and engineering stress in Fig. 2. Division of the whole uniaxial stress-strain relationship of HSS, in this paper, is into three stages: elastic stage, plastic stage, and coupled plastic-damage stage. The coupled plastic-damage stage is further decomposed into the plastic-dominated zone and the damage-dominated zone. The elastic stage is controlled by the elastic strain and elastic modulus. The plastic and coupled plastic-damage stages are presented in Fig. 3. Noted that the necking and damage effects are not considered in Fig. 3. The relationship of the uniaxial true stress-strain is easy to obtain in the plastic stage. The main discussion of this section focus on calculating the relationship of uniaxial true stress-strain in the coupled plastic-damage stage. Noted that the calibration process is in sequential order, the effects of the damage-dominated stage and multiaxial ductile fracture are not considered during parameter calibration in the plastic-dominated stage, and the effects of multiaxial ductile fracture are not considered during parameters calibration in the damage-dominated zone. To save computational time, the common J2 model in ABAQUS/Standard can be used in this section to calibrate the parameters.

Table 1
List of peak stress and plastic strain at the onset of necking.

Materials	Maximum true stress $\overline{\sigma}_u$ (MPa)	Corresponding plastic strain $\overline{\varepsilon}_u^p$
S700(A)	930.90	0.105
S700(B)	880.06	0.056
S960(A)	1117.10	0.060
S960(B)	1212.35	0.022

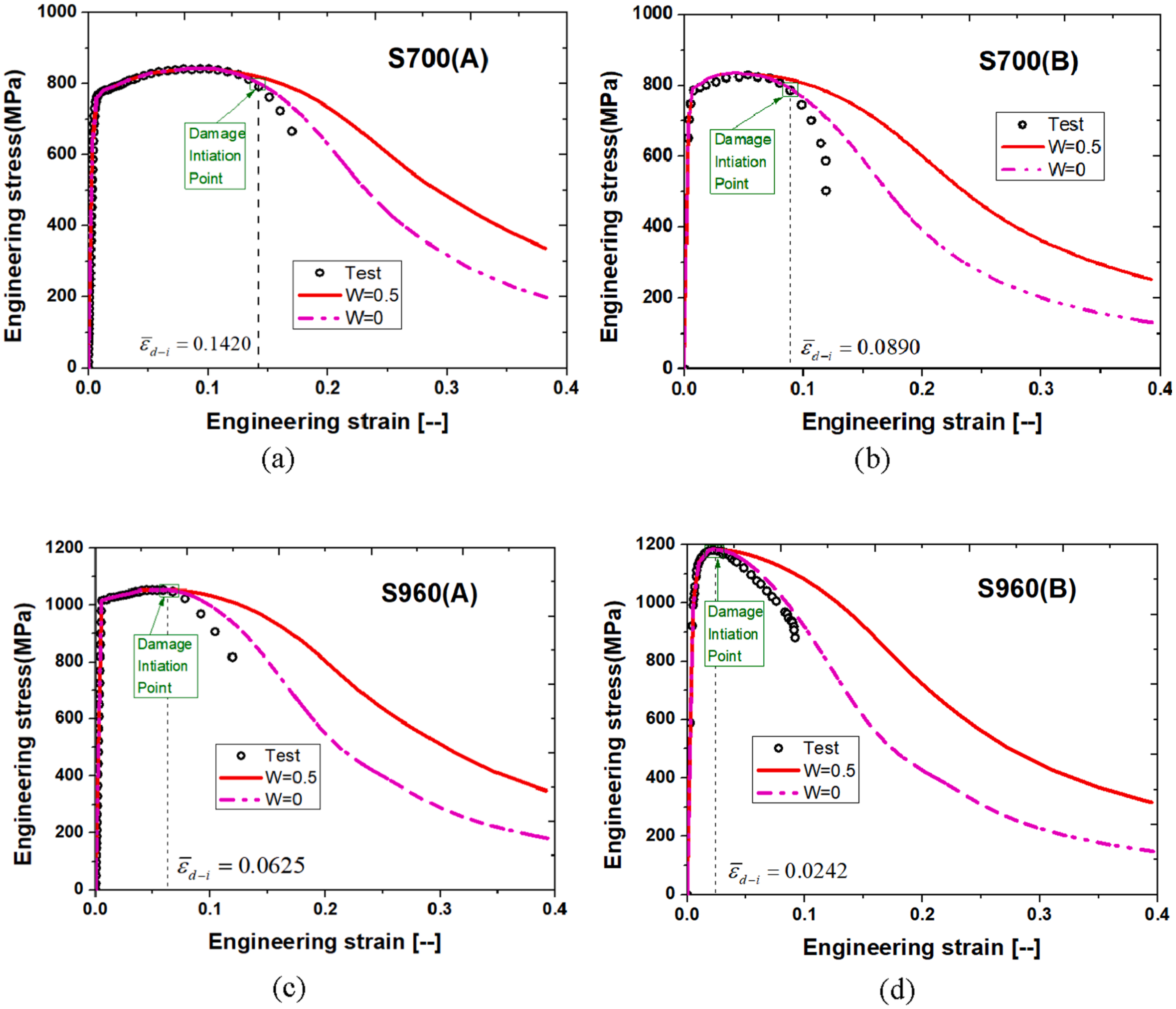

(a) (b) (c) (d)

Fig. 5. Calibration of weight constant beyond the necking.

The engineering strain ε_{en} - engineering stress σ_{en} relationship is converted to true stress σ -true strain ε relationship by equations 14 and 15. The relationship of true stress σ-true strain ε is further converted to true stress σ and plastic strain $\overline{\varepsilon}^p$ relationship. Fig. 4 presents the relationship between equivalent plastic strain and true stress without considering necking and damage effects.

$$\varepsilon = ln(1 + \varepsilon_{en}) \tag{14}$$

$$\sigma = \sigma_{en}(1 + \varepsilon_{en}) \tag{15}$$

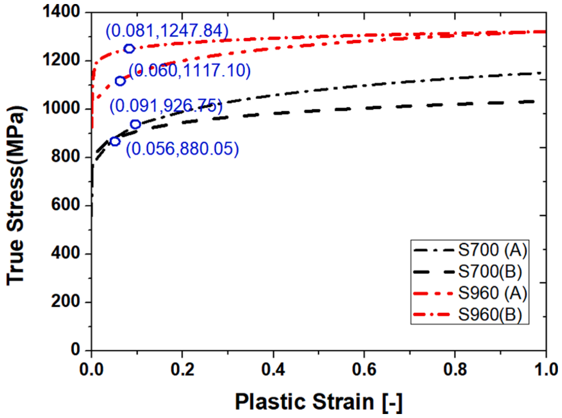

Fig. 6. True stress vs. plastic strain without considering damage (W = 0.0).

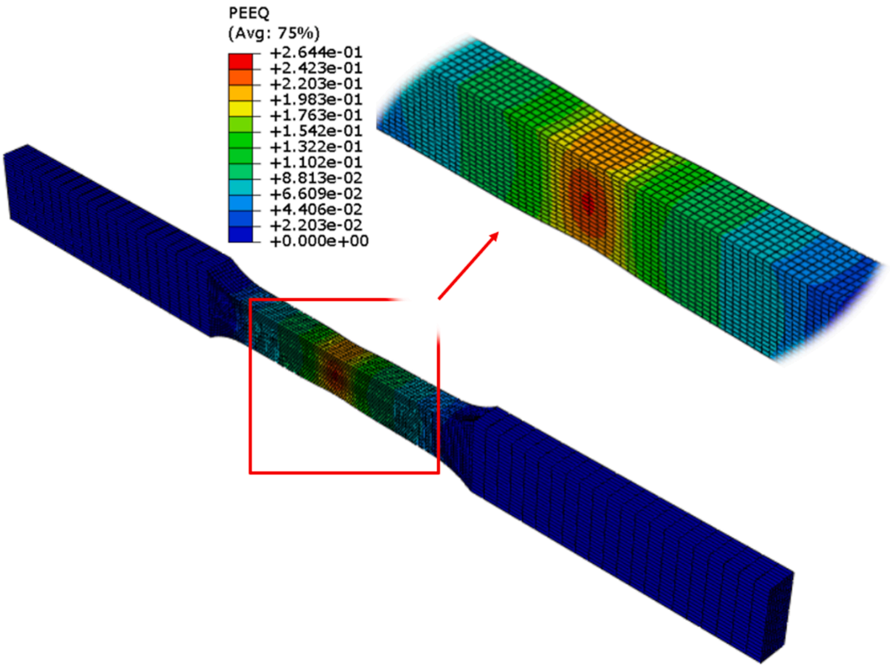

Fig. 7. Equivalent plastic distribution of S700(A) when $\overline{\varepsilon} = \overline{\varepsilon}_{d-i}$.

(1) Plastic stage

As shown in Fig. 3, the plastic stage is defined when $0 \leqslant \overline{\varepsilon}^p \leqslant \overline{\varepsilon}^p_u$. $\overline{\varepsilon}^p_u$ is the corresponding plastic strain when the true stress without considering necking and damage effects reached to the peak. In the plastic stage, the uniaxial plastic strain and true stress are simply obtained from the engineering strain - engineering stress relationship, see Fig. 4. The maximum true stress without considering necking and damage effects $\overline{\sigma}_u$ and corresponding plastic strain $\overline{\varepsilon}^p_u$ in Fig. 4 are listed in Table 1 for various steel types considered.

(2) Plastic-dominated zone of coupled plastic-damage stage

As shown in Fig. 3, when $\overline{\varepsilon}^p_u > \overline{\varepsilon}^p$, the coupled plastic-damage stage reached. The point of maximum true stress is the onset of the necking, see Fig. 4. When $\overline{\varepsilon}^p_u < \overline{\varepsilon}^p \leqslant \overline{\varepsilon}^p_{d-i}$ the plasticity is dominated in the coupled plastic-damage stage. There are several alternatives to predict post-necking behavior, such as the Ramberg-Osgood relationship [30], a combined power-exponential law [17,18], and the

Table 2
List of true stress and plastic strain at damage initiation.

Materials	Plastic strain at damage initiation $\bar{\varepsilon}^p_{d-i}$	Corresponding stress $\bar{\sigma}_{d-i}$
S700(A)	0.264	1017.16
S700(B)	0.243	955.17
S960(A)	0.060	1117.10
S960(B)	0.081	1247.84

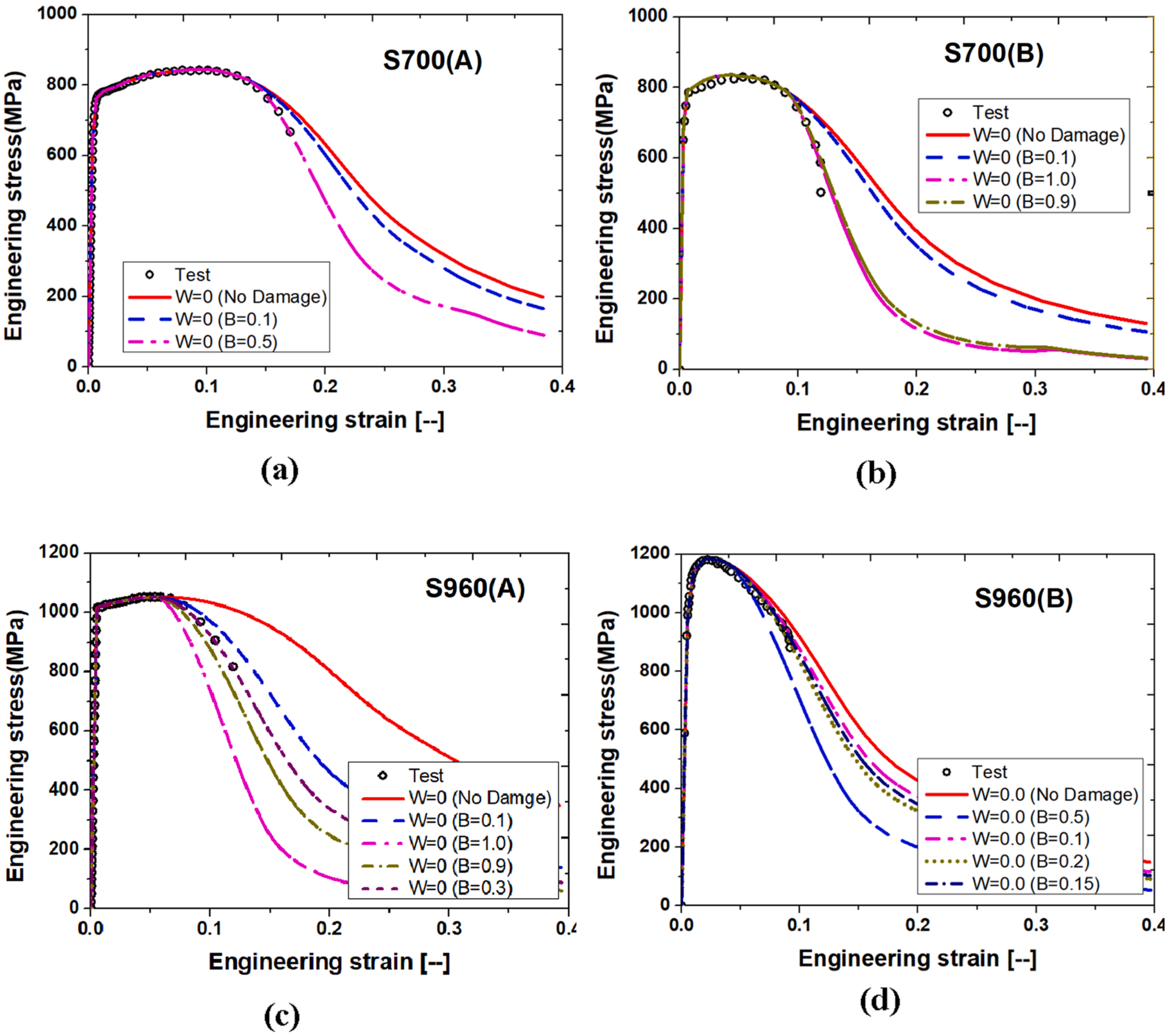

Fig. 8. Calibration of damage parameter B of damage-dominated coupled plastic-damage stage.

weighted average model [31]. The weighted function [31], as expressed in Eq.(16), is used to predict the true stress after necking. The weight constant W could be determined through calibration. The measured engineering stress-engineering strain relationship is considered as a target, the weight constant W is varied in the finite element model (presented in Fig. 5) until the calculated engineering stress-engineering strain relationship meets a required accuracy.

$$\bar{\sigma}^{neck} = \bar{\sigma}_u \left[W\left(1 + \bar{\varepsilon}^p - \bar{\varepsilon}^p_u\right) + (1 - W)\left(\frac{\left(\bar{\varepsilon}^p\right)^{\bar{\varepsilon}^p_u}}{\left(\bar{\varepsilon}^p_u\right)^{\bar{\varepsilon}^p_u}}\right)\right] \tag{16}$$

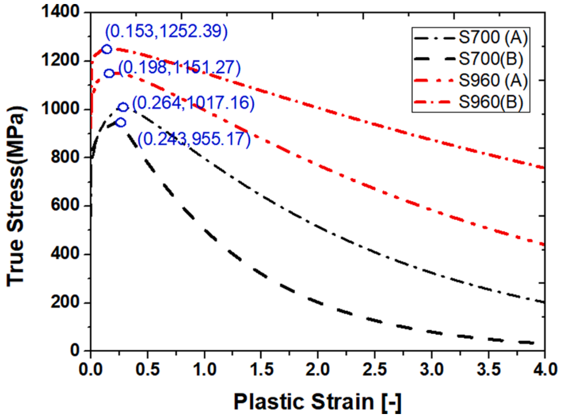

Fig. 9. The relationship between equivalent plastic strain and true stress for J2 plasticity model.

Table 3
List of true stress, corresponding plastic strain, damage variable of Fig. 9 when true stress reached the peak.

Materials	True stress $\overline{\sigma}_f$	Plastic strain $\overline{\varepsilon}_f^p$	Damage variable d	Damage Parameter B
S700(A)	1017.16	0.264	0.00	0.5
S700(B)	955.17	0.243	0.00	0.9
S960(A)	1151.27	0.198	0.04	0.3
S960(B)	1252.39	0.153	0.01	0.2

Where: W is a weight constant, $0\leqslant W\leqslant 1$.

The calibration process is suggested to start with a weight constant W = 0.5. If the calculated engineering stress is larger than the test results, the weight constant should be reduced in the following range: $0\leqslant W<0.5$. If the calculated engineering stress is smaller than the test results, the weight constant should be increased in the following range: $0.5<W\leqslant 1.0$. After then, we can continue to calibrate the weight constant with a smaller range.

The stop criterion for the calibration of the weight constant W for structural steels is in the following two situations: The calculated engineering stress is larger than test results when the constant W is 0.0, indicating that this material is less ductile. The predicated engineering stress agreed well with test results when $\overline{\varepsilon}_u<\overline{\varepsilon}\leqslant\overline{\varepsilon}_{d-i}$ but gives a relatively larger prediction when the $\overline{\varepsilon}>\overline{\varepsilon}_{d-i}$. ② The weight constant W, $0\leqslant W\leqslant 1$, make the calculated engineering stress agreed well with test results when $\overline{\varepsilon}_u<\overline{\varepsilon}\leqslant\overline{\varepsilon}_{d-i}$, but gives a relatively larger prediction when the $\overline{\varepsilon}>\overline{\varepsilon}_{d-i}$. The calibration of the weight constant W is stopped when increasing or decreasing W will make the predicted results far away from the experimental data when $\overline{\varepsilon}_u<\overline{\varepsilon}\leqslant\overline{\varepsilon}_{d-i}$. It is not common for the structural steels to get a weight constant W as 1.0. The point $\overline{\varepsilon}=\overline{\varepsilon}_{d-i}$ is defined as the onset of the damage-dominated zone of the coupled plastic-damage stage. The corresponding maximum plastic strain, in the finite element model, is defined as the equivalent plastic strain at the onset of the damage-dominated zone $\overline{\varepsilon}_{d-i}^p$ of the coupled plastic-damage stage, see Fig. 3.

The calibration of weight constant after the necking period of S700 and S960 is shown in Fig. 5. Because steel S700 and S960 are less ductile, the weight constant W of both steel grades is calibrated as zero. The point $\overline{\varepsilon}=\overline{\varepsilon}_{d-i}$ is marked in Fig. 5 as the damage initiation point. The relationship between true stress and equivalent plastic strain without considering the damage is shown in Fig. 6. The equivalent plastic strain at the onset of the damage-dominated zone $\overline{\varepsilon}_{d-i}^p$ is determined as the maximum equivalent plastic strain based on the finite element simulation when the engineering strain is reached $\overline{\varepsilon}=\overline{\varepsilon}_{d-i}$. The equivalent plastic strain distribution of S700(A) steels is presented in Fig. 7 as an example when $\overline{\varepsilon}=\overline{\varepsilon}_{d-i}$. The $\overline{\varepsilon}_{d-i}^p$ is calibrated as 0.2644 for S700(A) steels. The summary of $\overline{\varepsilon}_{d-i}^p$ and corresponding stress is listed in Table 2.

(3) Damage-dominated zone of coupled plastic-damage stage

When $\overline{\varepsilon}^p>\overline{\varepsilon}_{d-i}^p$ the damage is dominated in the coupled plastic-damage stage. The true stress in the damage-dominated zone could be obtained through Eq.(17). The damage evolution law, expressed in Eq.(18), is adopted to determine the dependence of the damage scalar d on the equivalent plastic strain $\overline{\varepsilon}^p$. The parameter B is also determined using the calibration method. The measured engineering stress-engineering strain relationship is considered as a target, the parameter B is varied in the finite element model (shown in Fig. 5) until the calculated engineering curves agree well with the experimental results.

$$\overline{\sigma}=(1-d)\overline{\sigma}^{neck} \tag{17}$$

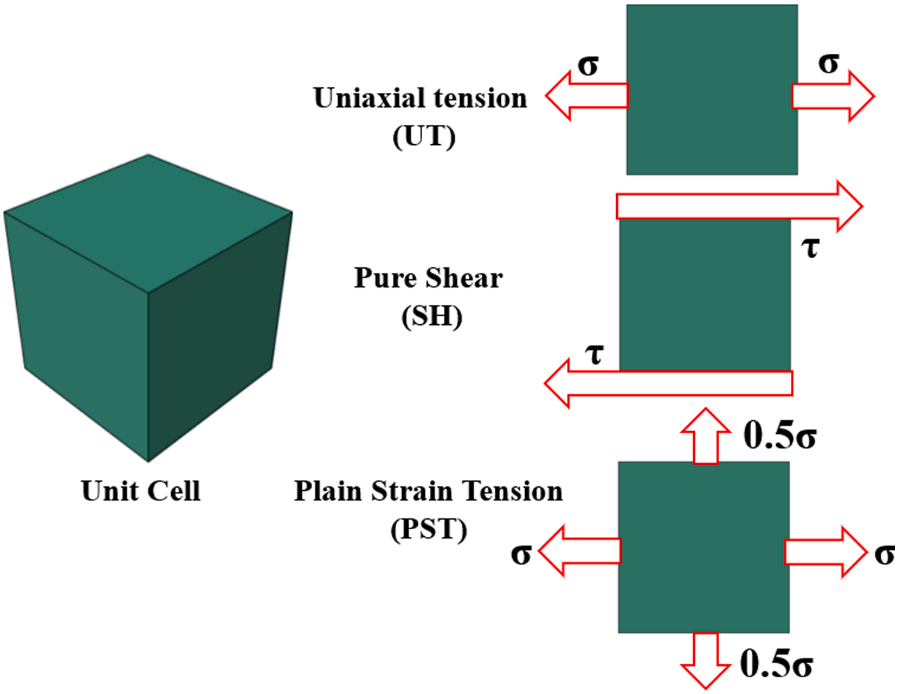

Fig. 10. Virtual Multiaxial loading using computational homogenization.

$$d = \begin{cases} 0 & \bar{\varepsilon}^p < \bar{\varepsilon}^p_{d-i} \\ 1 - exp\left[- B\left(\bar{\varepsilon}^p - \bar{\varepsilon}^p_{d-i} \right) \right] & \bar{\varepsilon}^p \geqslant \bar{\varepsilon}^p_{d-i} \end{cases} \tag{18}$$

Where: B is model parameters of damage evolution law.

Fig. 8 presented the calibration process of damage parameter B. The optimized value of damage parameter B is 0.5 for S700(A), 0.9 for S700(B), 0.3 for S960(A), and 0.2 for S960(B). The relationship between equivalent plastic strain and true stress for the isotropic hardening J2 plasticity model is shown in Fig. 9. The maximum true stress, corresponding true strain, and corresponding damage variable d is listed in Table 3.

3.2. Ductile fracture parameter identification

The fracture parameters of the Hosford-Coulomb fracture model could be determined based on uniaxial tension (UT) fracture strain $\bar{\varepsilon}^p_{UT}$, in-plane shear fracture strain (SH) $\bar{\varepsilon}^p_{SH}$, and plane strain tension (PST) fracture strain $\bar{\varepsilon}^p_{PST}$. It is straightforward to identify the parameters of the Hosford-Coulomb model based on the following three steps procedure according to [17,18].

☐ Determine parameter "b" from UT fracture strain [17,18]:

$$b = \bar{\varepsilon}^p_{UT} \tag{19}$$

☐ Determine parameter "c" from PST and SH fracture strain [17,18]:

$$c = \frac{1 - \left(\frac{\bar{\varepsilon}^p_{PST}}{\bar{\varepsilon}^p_{SH}} \right)^n}{\frac{2}{\sqrt{3}} \left(\frac{\bar{\varepsilon}^p_{PST}}{\bar{\varepsilon}^p_{UT}} \right)^n + \left(\frac{\bar{\varepsilon}^p_{PST}}{\bar{\varepsilon}^p_{SH}} \right)^n - 1} \tag{20}$$

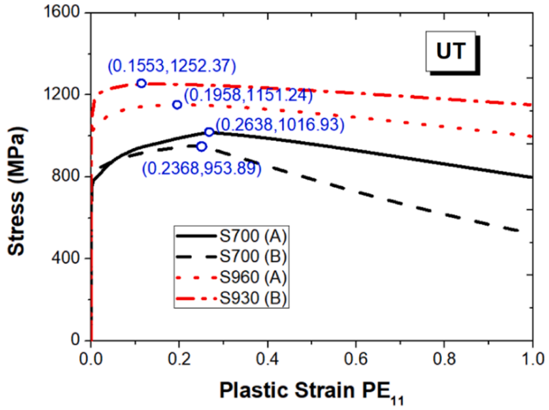

(a) Uniaxial tension, $\bar{\varepsilon}_{11}^{p}$ vs. true stress

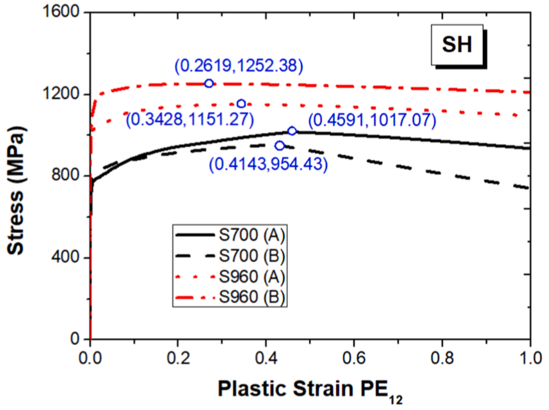

(b) Pure shear, $\bar{\varepsilon}_{12}^{p}$ vs. true stress

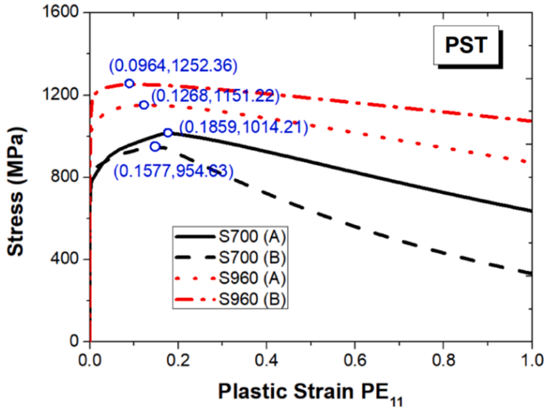

(c) Plain strain tension, $\bar{\varepsilon}_{11}^{p}$ vs. true stress

Fig. 11. Relationship between stress and plastic strain under different stress status.

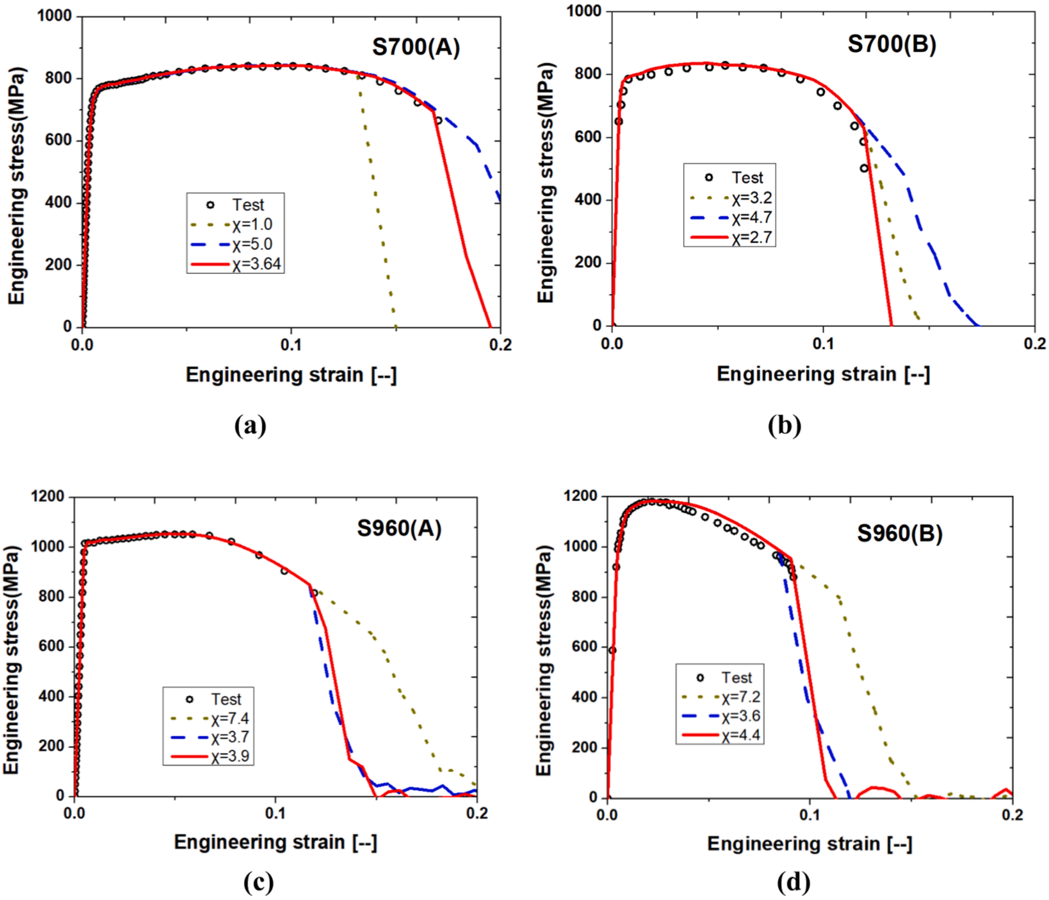

(a) (b) (c) (d)

Fig. 12. Calibration of the rescaling parameter χ for the fracture plastic strain.

Table 4
Parameters of Ductile fracture model.

Materials	$\bar{\varepsilon}^p_{UT}$	$\bar{\varepsilon}^p_{SH}$	$\bar{\varepsilon}^p_{PST}$	a	b	c	χ
S700(A)	0.2638	0.4590	0.1859	1.6208	0.2638	0.0840	3.7
S700(B)	0.2368	0.4143	0.1577	1.5660	0.2368	0.0906	2.7
S960(A)	0.1958	0.3428	0.1268	1.5413	0.1958	0.0936	3.9
S960(B)	0.1553	0.2619	0.0964	1.5017	0.1552	0.0946	4.4

Where: the exponent n is recommended to be 0.1 according to [17,18].

 Determine the exponent “a” from solving equation 21. The parameter “a” is recommended between 1 and 2 to guarantee the uniqueness of the solution [17,18].

$$\left(1+2^{a-1}\right)^{1/a} = \sqrt{3}(1+c)\left(\frac{\bar{\varepsilon}^p_{UT}}{\bar{\varepsilon}^p_{SH}}\right)^n \tag{21}$$

The fracture strain under uniaxial tension (UT) $\bar{\varepsilon}^p_{UT}$, in-plane shear (SH) $\bar{\varepsilon}^p_{SH}$, and plane strain tension (PST) $\bar{\varepsilon}^p_{PST}$ are generally recommended to be obtained directly from experiments [17,18]. Computational homogenization is used to generate different stress states by the virtual multiaxial loading, as shown in Fig. 10, to alleviate the extra requirements on the number of experiments. The detailed explanation of computational homogenization and periodic boundary conditions is referred to the authors’ previous publication [32,33]. As shown in Fig. 11, the relationship between the equivalent true stress and plastic strain component under different stress status is predicted by virtual multiaxial loading.

The computational homogenization leads to the relationship between stress and plastic strain under different stress status, the

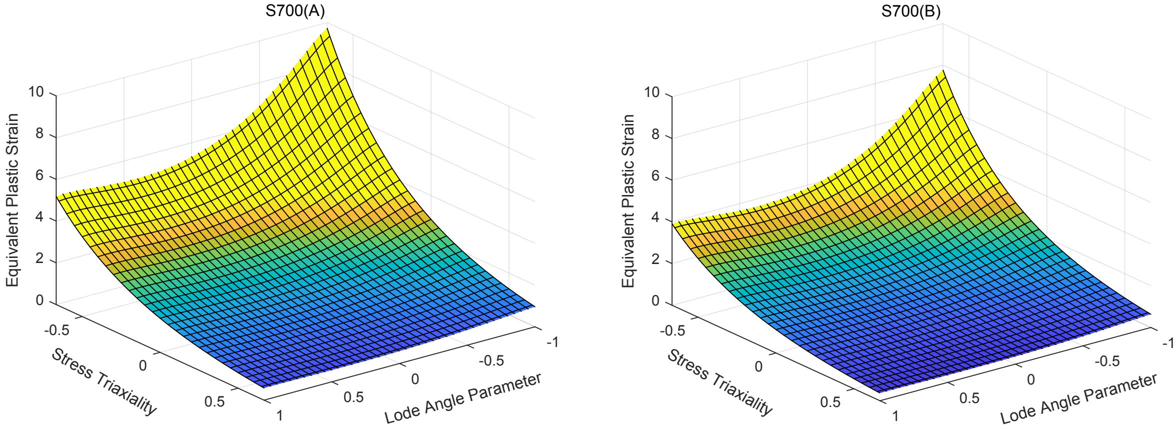

(a) S700(A) (b) S700(B)

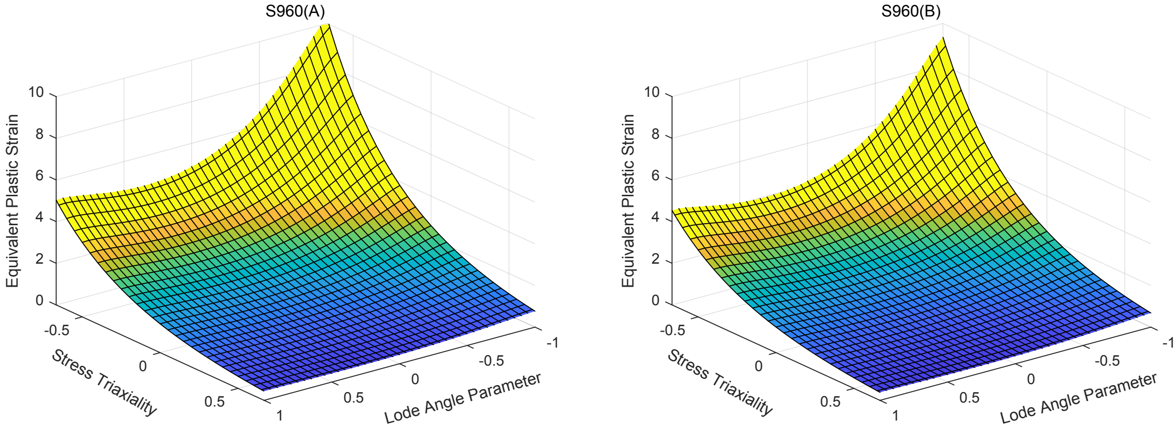

(c) S960(A) (d) S960(B)

Fig. 13. Equivalent plastic strain to fracture as a function of the stress state.

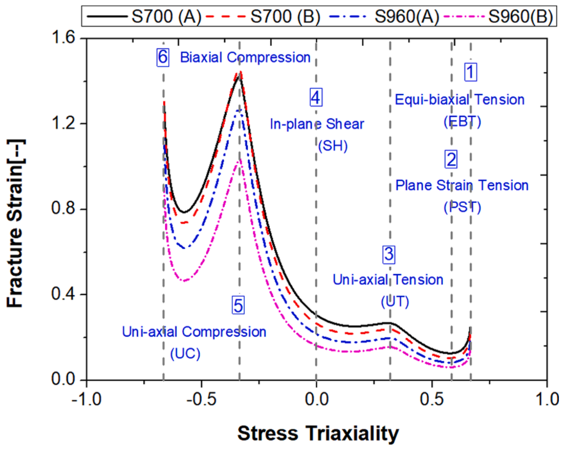

Fig. 14. 2D View of equivalent plastic strain to fracture vs. stress triaxiality.

Table 5
Fracture strain at different stress status.

Steel Grade	$\bar{\varepsilon}^p_{EBT}$	$\bar{\varepsilon}^p_{PST}$	$\bar{\varepsilon}^p_{UT}$	$\bar{\varepsilon}^p_{SH}$	$\bar{\varepsilon}^p_{UC}$	$\bar{\varepsilon}^p_{EBC}$
S700(A)	0.9033	0.4646	0.9033	1.1050	5.1749	4.7356
S700(B)	0.5904	0.2811	0.5904	0.7077	3.9037	3.4935
S960(A)	0.7115	0.3276	0.7115	0.8461	5.0220	4.4465
S960(B)	0.6241	0.2733	0.6241	0.7085	4.5296	3.9336

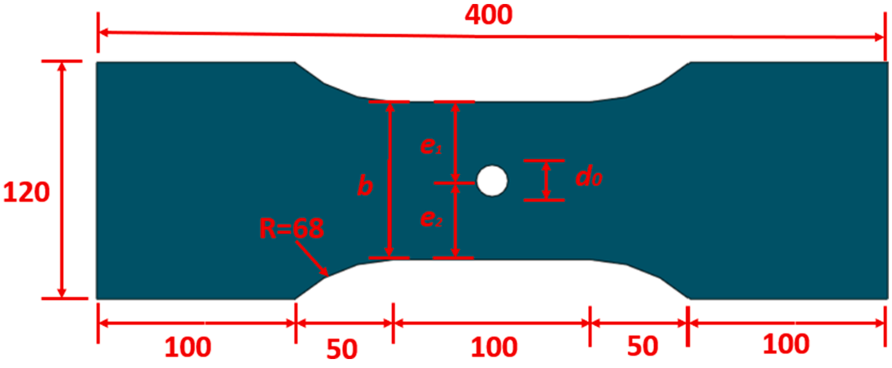

Fig. 15. Geometry illustration (Unit:mm).

Table 6
Geometry of specimens (Unit: mm).

Steel Grade	Nominal Diameter of Middle Holes	b	t	d_0	e_1	e_2
S700(A)	0	76.95	8.02	–	–	–
	8	76.12	7.86	7.79	37.86	38.26
	16	76.10	7.95	15.64	38.29	37.81
	24	76.04	7.94	23.61	38.20	37.84
	32	76.05	7.92	31.59	37.94	38.11
	40	75.78	7.93	39.50	38.07	37.71
S960(A)	0	79.55	8.07	–	–	–
	8	80.03	8.08	7.79	40.17	39.86
	16	80.06	8.04	15.64	40.08	39.98
	24	80.03	8.08	23.61	40.18	39.85
	32	80.16	8.08	31.59	40.17	39.99
	40	79.72	8.03	39.50	39.95	39.77
S700(B)	8	80.20	7.93	7.86	40.55	39.65
	16	80.11	7.91	15.85	40.36	39.75
	24	80.07	7.97	23.76	40.44	39.63
	32	80.11	7.86	31.87	40.39	39.72
	40	80.20	7.88	39.77	40.38	39.82
S960(B)	8	80.07	7.97	7.92	40.52	39.55
	16	79.96	8.11	15.92	40.46	39.50
	24	80.11	8.04	23.41	40.47	39.64
	40	80.09	8.04	40.58	40.19	39.90

fracture point is still unknown. Thus, it is proposed here that the fracture strain is a proportional rescaling of the equivalent plastic strain $\bar{\varepsilon}^p_{peak}$ when the true stress reaches the maximum value. The fracture strain could be expressed as $\chi\bar{\varepsilon}^p_{peak}$. χ is defined as a rescaling parameter. The plastic strain $\bar{\varepsilon}^p_{peak}$ is extracted from Fig. 11. The ductile fracture parameters of the Hosford-Coulomb fracture model could be obtained based on Equations (19)–(21). The rescaling parameter χ is obtained through the calibration similar to the weight constant W and the damage parameter B in Section 3.1 above. The calibration process of the rescaling parameter χ is shown in Fig. 12. The initial assumption of the rescaling parameter χ is suggested as the ratio of the maximum equivalent plastic strain between peak true stress and the final fracture during calibration of damage parameter B in Fig. 8. The final parameters of the ductile model are summarized in Table 4, for both steel grades.

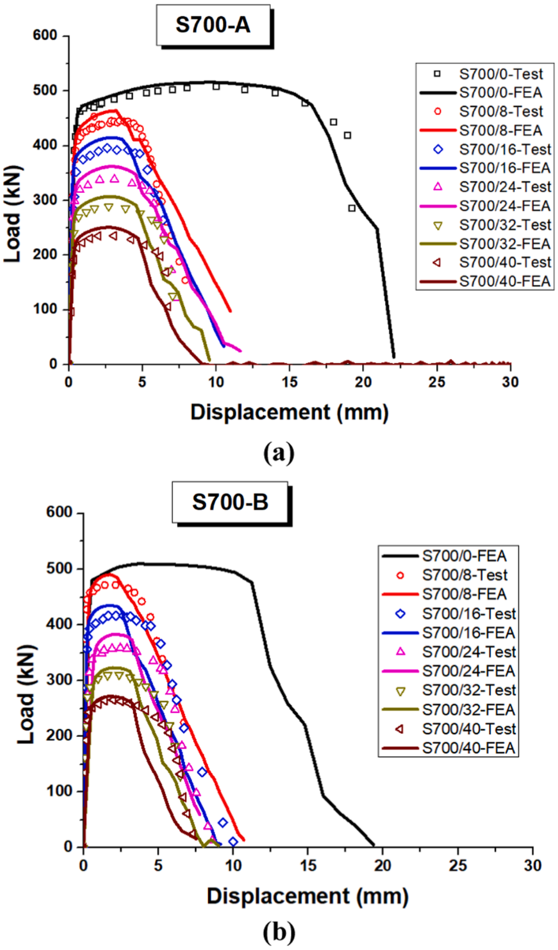

Fig. 16. Comparisons between FE and experimental results of S700.

The equivalent plastic strain to fracture is a function of the stress state, see Fig. 13. For plane stress conditions, the Lode angle parameter is a function of the stress triaxiality as shown in Eq. (13). The fracture strain of the Hosford-Coulomb model could be conveniently transferred to the 2D view, as shown in Fig. 14. The equivalent plastic strains to fracture exposed to uniaxial tension (UT), plane strain tension (PST), equi-biaxial tension (EBT), in-plane shear (SH), uniaxial compression (UC) and equi-biaxial compression (EBC) are listed in Table 5.

$$\bar{\theta} = 1 - \frac{2}{\pi}\arccos\left[-\frac{27}{2}\eta\left(\eta^2-\frac{1}{3}\right)\right] \quad -\frac{2}{3}\leqslant\eta\leqslant\frac{2}{3} \tag{13}$$

4. Validation of numerical simulation

The implemented uncoupled ductile fracture model in Section 2 and identified fracture parameters in Section 3 are validated by the HSS plate with different hole sizes (0, 8, 16, 24, 32, and 40 mm) reported in [24]. The detailed geometry of HSS plates with holes is shown in Fig. 15 and Table 6. The force-displacement curve comparisons and failure modes between FE and experiments are shown in Fig. 16 and Fig. 17, and in Fig. 18 respectively. A good agreement using the material models presented above is observed. The crack pattern from FE agreed well with test results, leading to the conclusions that the proposed modeling strategy is successfully validated. Noted that the calibrated parameter is not validated by shear-dominated failure mode due to a lack of experimental data.

The comparisons in Fig. 18 is quantified based on Eq. (14) and (15) by comparing the force at the same displacement in the softening stage between experiments and FE. The root mean error (RME) and maximum error (EMAX) between tests and FE are summarized in Table 7. The average RME is around 10% and 15% for steel from producer A and B, respectively. The average EMAX is between 30% and 37% because the error is more sensitive to the force when the force becomes smaller. Noted that the prediction accuracy highly depended on the uniaxial stress-strain curves provided by the producer. The proposed strategies to predict the fracture

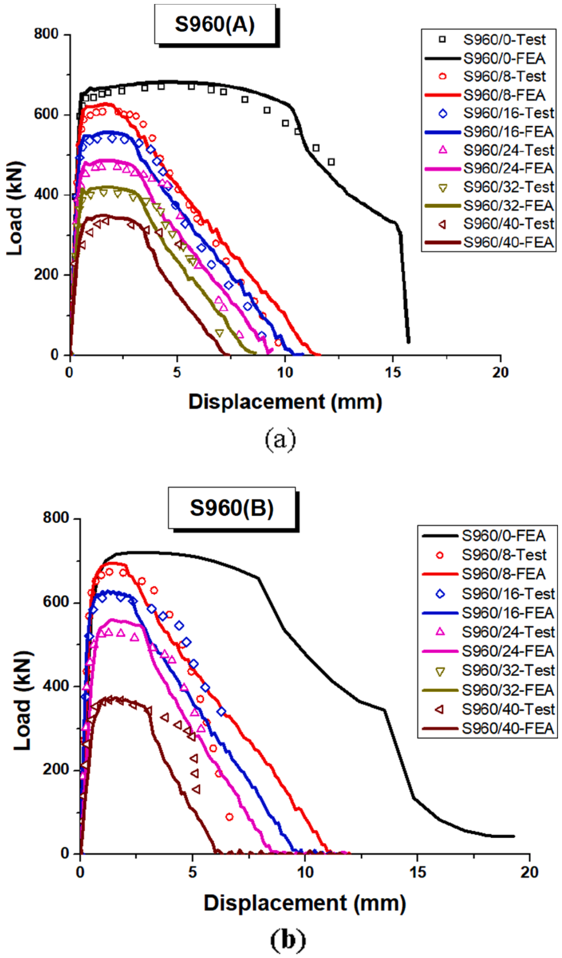

Fig. 17. Comparisons between FE and experimental results of S960.

of HSS using the uniaxial stress-strain curve could be an alternative in engineering applications.

$$RME = \frac{1}{n}\sum_{i=1}^{n}\frac{|P_{test,i} - P_{FE,i}|}{P_{test,i}} \qquad \mathrm{i = 1 \ldots n} \tag{14}$$

$$EMAX = MAX\left(\sum_{i=1}^{n}\frac{|P_{test,i} - P_{FE,i}|}{P_{test,i}}\right) \qquad \mathrm{i = 1 \ldots n} \tag{15}$$

Where: $P_{test,i}$ and $P_{FE,i}$ is the experimental force and predicted force at the same displacement. The displacement is taken in the softening stage with an increment of 1 mm, from the peak force to the final fracture.

The specimens without and with a 40 mm hole made of S700(A) and S960(A) are selected to show the progressive failure process, see Fig. 19 and Fig. 20. The necking in the center of the specimen leads to a triaxial stress state when the displacement is 16.5 mm and 10.6 mm for S700(A)/0 and S960(A)/0, respectively. At this stage, the void nucleation and growth would happen. Upon further loading, the crack is initiated in the center of the specimen when the displacement is 17.6 mm and 10.8 mm for S700(A)/0 and S960 (A)/0, respectively. The crack is gradually propagated when the displacement increased to 20.9 mm and 14.9 mm for S700(A)/0 and S960(A)/0, respectively, and a deformation band is at around 45^0 inclined to the longitudinal axes of the dog-bone specimen. The strain concentration in the deformation bands is causing the crack pattern along confined to the deformation bands, at 22.1 mm and 14.9 mm for S700(A)/0 and S960(A)/0, respectively.

For the specimen with a 40 mm hole in the middle, as shown in Figs. 21 and 22, the crack initiated in the inner side of the hole due to the stress concentration, and gradually propagated toward outside until the specimen is fractured. The crack surface of S700(a)/40 is smooth, but the crack surface of S960(A)/40 has a stripe pattern.

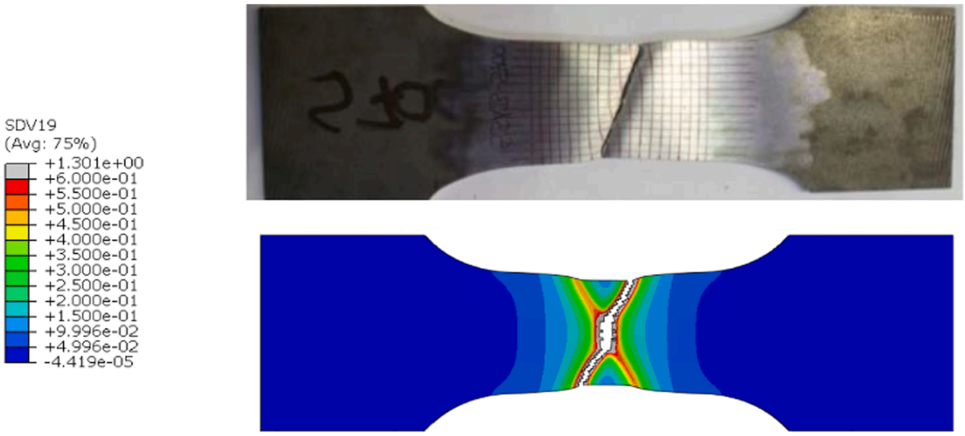

(a) S700(A)/0

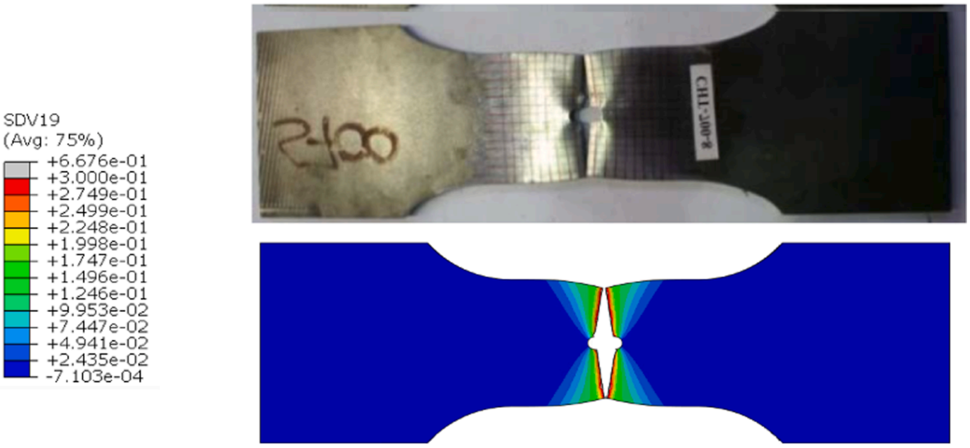

(b) S700(A)/8

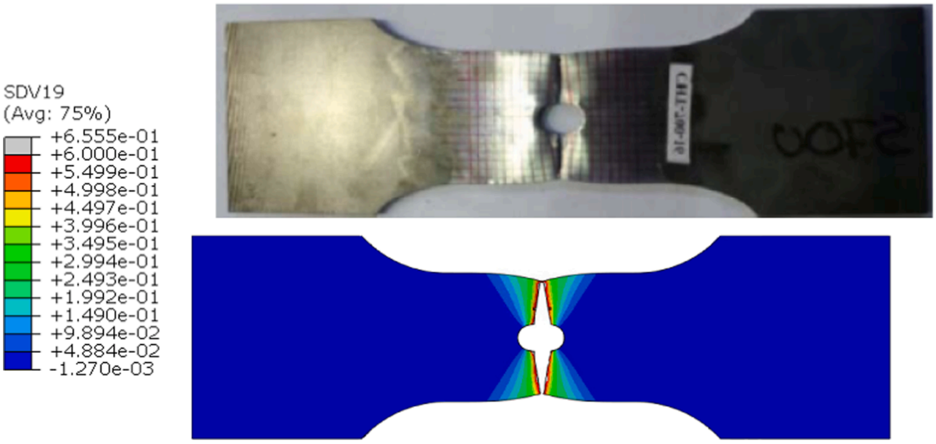

(c) S700(A)/16

Fig. 18. Failure mode comparisons between FE and experiments of S700(A) (SDV19: Equivalent plastic strain).

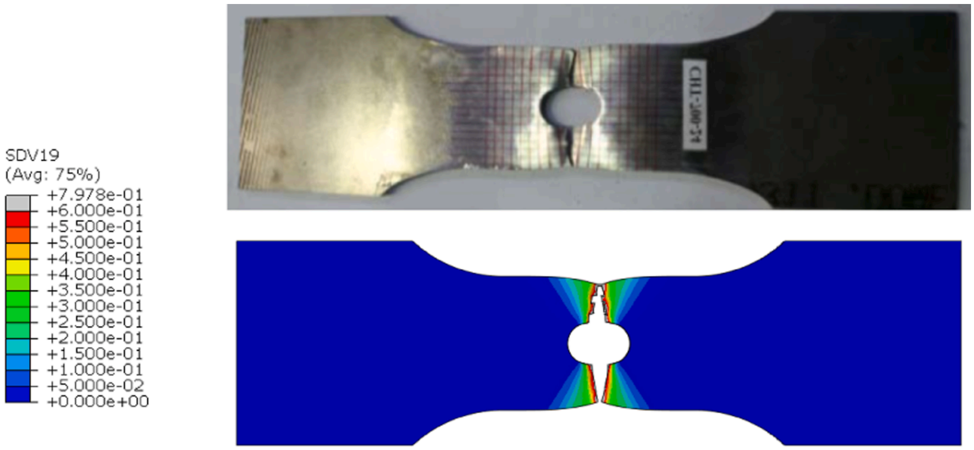

(d) S700(A)/24

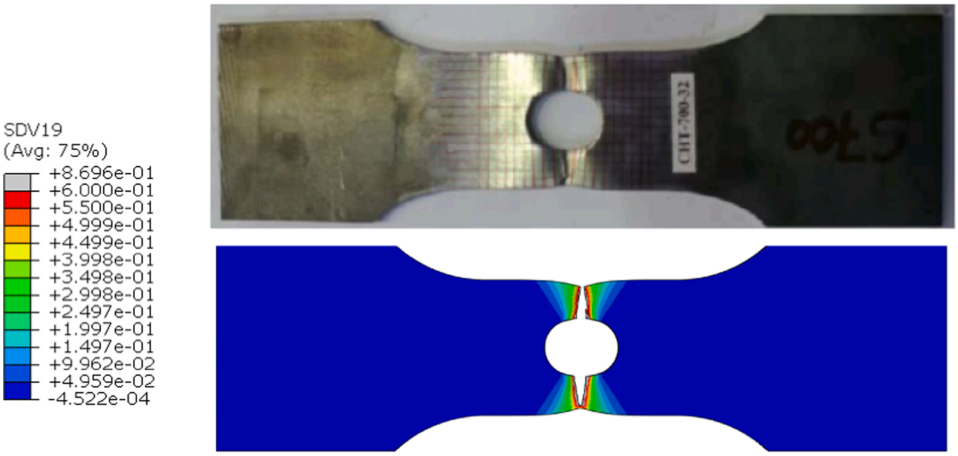

(e) S700(A)/32

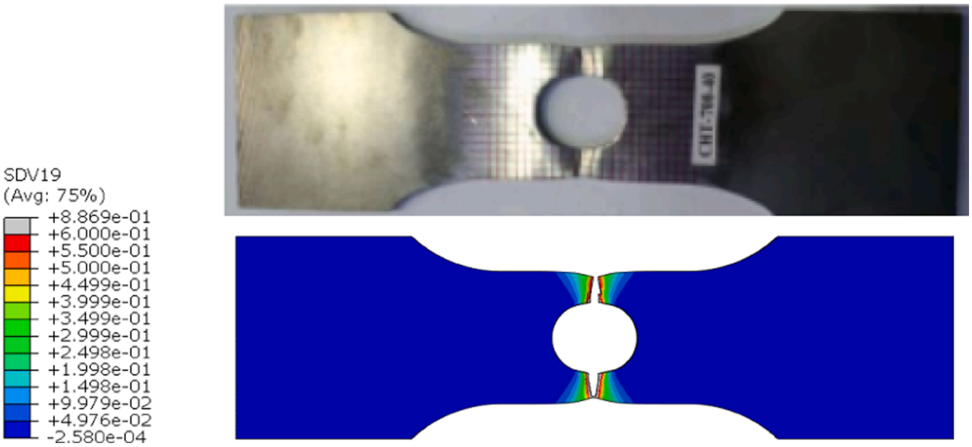

(e) S700(A)/40

Fig. 18. (*continued*).

Table 7
Root mean error (RME) and maximum error (EMAX) between tests and FE (Unit: mm).

Hole Size	Steel Grades							
	S700(A)		S700(B)		S960(A)		S960(B)	
	RME	EMAX	RME	EMAX	RME	EMAX	RME	EMAX
0	4.0%	15.1%	–	–	4.8%	8.6%	–	–
8	15.0%	58.7%	4.8%	8.4%	7.6%	26.3%	18.6%	65.7%
16	5.6%	9.0%	19.1%	34.9%	11.2%	23.3%	13.0%	20.4%
24	10.7%	39.5%	17.7%	35.5%	11.0%	29.8%	8.0%	15.2%
32	12.8%	28.9%	16.2%	34.1%	15.3%	47.2%	–	–
40	11.9%	40.4%	19.8%	45.5%	14.7%	46.4%	23.8%	46.4%
Average	10.0%	31.9%	15.5%	31.6%	10.7%	30.2%	15.8%	36.9%

5. Case study

FE simulations are performed on a single K gap joint made of square cold-formed hollow sections. Solid elements C3D8 are used to model nominal cross-section properties of RHS and weld material. The coupon test results reported in the RUOSTE project [24] are assumed constant in all parts of the cross-sections and in weld material which is the major simplification of FEA. This means that no effects of cold forming on corners nor the effects of material change due to welding (HAZ) are modeled. Such assumptions would lead to the overestimation of deformation capacity and possible resistance of the joint. This fact is ignored in the case study because the focus is on analyzing and quantifying the effects of the damage material model and the numerical estimate of the fracture strain at a multiaxial loading state on the joint resistance and deformation capacity. Four material properties of two steel grades presented in Section 3 are used in the parametric study of the joint behavior to predict the ultimate resistance and deformation capacity of the K gap joints. The basic material properties are shown in Table 8.

Prerequisites according to ratio ultimate strength/yielding strength and minimum fracture strain are defined for steel grades up to S700 according to EN1993-1-1 [34]. The distinction is made depending on the structural global analysis as follows: for elastic global analysis is that $f_u/f_y \geqslant 1.05$ and $\varepsilon_A \geqslant 12\%$. For plastic global analysis, the prerequisites are more demanding so the following values are imposed $f_u/f_y \geqslant 1.10$ and $\varepsilon_A \geqslant 15\%$. Clearly, only S700(A) could satisfy the criteria for use in joint resistance according to the global plastic theory. The main goal of the FE analysis is to estimate the difference in the joint resistance predicted using three levels of complexity for the material model:

- Elastic-Plastic-Hardening (EPH) model. The true stress-strain relationship is based on eq. (14 and 15), see Fig. 4. The model provides realistic assumptions until the plastic strain, $\overline{\varepsilon_u}^p$. The necking effects are not considered.
- Elastic-Plastic-Hardening including the damage parameter (EPHD) model. The true stress-strain relationship is based on Fig. 9. The model provides realistic assumptions until fracture but overestimates true strains because no fracture criterion is considered.
- Elastic-Plastic-Hardening-Damage-Fracture including calibrated multiaxial fracture strain (EPHDF) model. The true stress-strain relationship is the most realistic because the fracture strain limit is considered and the deletion of the elements from the finite element mesh is introduced in FEA. Material properties are based on parameters of the ductile fracture model shown in Table 4.

The nominal geometrical variables of the K gap joint are shown in Fig. 23 and listed in Table 9. The cross section of chord and brace are both square. The length of each member is set to 5 times the members' width, b_i, to ensure that the stresses at the joint zone are not influenced by the boundary conditions. Both brace members are made with the same cross-section and have the same inclination, $\theta_i = 30^0$. The parameter β representing the brace width to the chord width ratio is 0.5. The fillet weld thickness t_w is calculated as the full strength weld depending on the brace thickness t_o and the yield strength of the material f_y. The finite element mesh and boundary conditions are illustrated in Fig. 24. One end of the chord is pinned, and the other end is free. One brace member is pinned, and the other brace member is roller pinned to allow the translation in the axial direction. The boundary condition and the load are applied using the MPC constraints where the center of the member is the reference point and the chord end surface is the slave surface.

The load-deformation curves of K gap joints made of S700(A) and S700(B) are shown in Fig. 25. The deformation is defined as the ratio of the relative axial displacement of the loaded brace d to the gauge length $h_0/\sin\theta$. The characteristic resistance of K gap joints made of S700 is calculated as 607.4kN, considering material factor $C_f = 0.8$ based on the latest proposed new version of European standard, EC3 part 1-8 chapter 9 [35]. The force at 3% deformation is almost identical, 911.2 kN, for K gap joint using material properties S700(A)-EPH, S700(A)-EPFD, and S700(A)-EPHDF models. The characteristic resistance is 0.67 at 3% deformation for K gap joints using material properties S700(A). There is no influence on the joint resistance due to the relatively large engineering fracture strain of S700(A) (17.0%), while the deformation capacity is smaller up to 20% if the most sophisticated material model is used, see Fig. 25.a.

The force at 3% deformation or the maximum force is 888.6 kN, 933.6 kN, 919.8 kN for K gap joint using material properties S700(B)-EPH, S700(B)-EPHD, and S700(B)-EPHDF, respectively. The characteristic resistance is 0.68, 0.65 and 0.66 of the joint resistance at 3% deformation using material properties S700(B)-EPH, S700(B)-EPHD, and S700(B)-EPHDF, respectively. The influence of lower

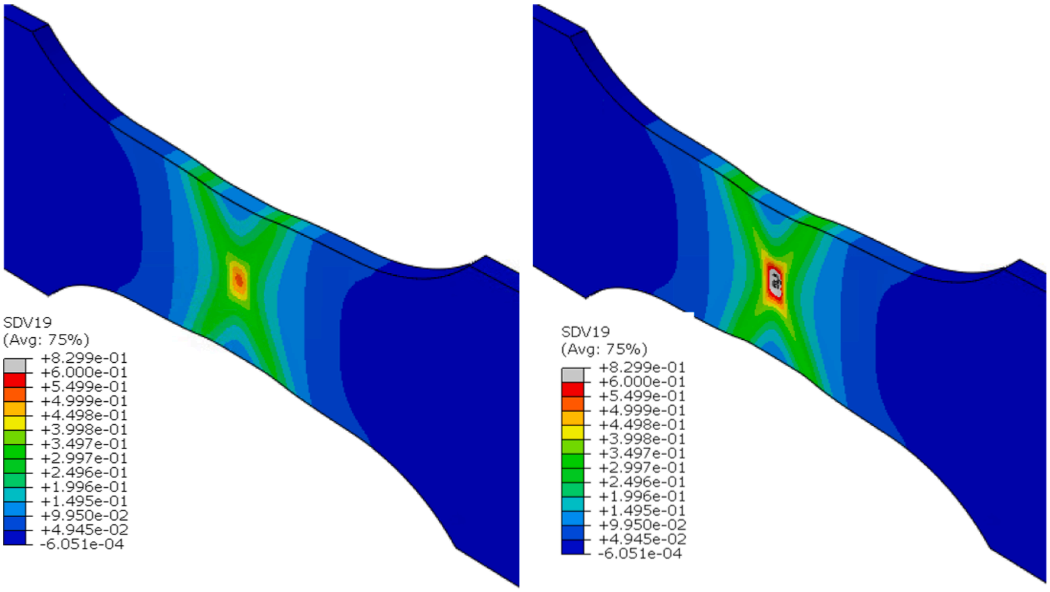

(a) Displacement=16.5mm (b) Displacement =17.6mm

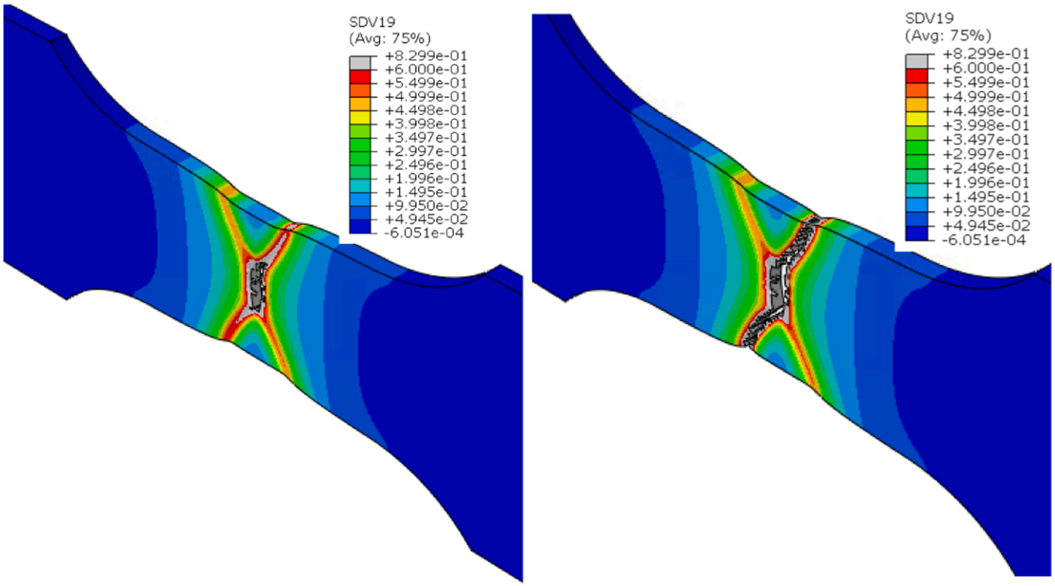

(c) Displacement =20.9mm (d) Displacement =22.1mm

Fig. 19. Failure Process and equivalent plastic strain distribution of S700(A)/0 (SDV19: Equivalent plastic strain).

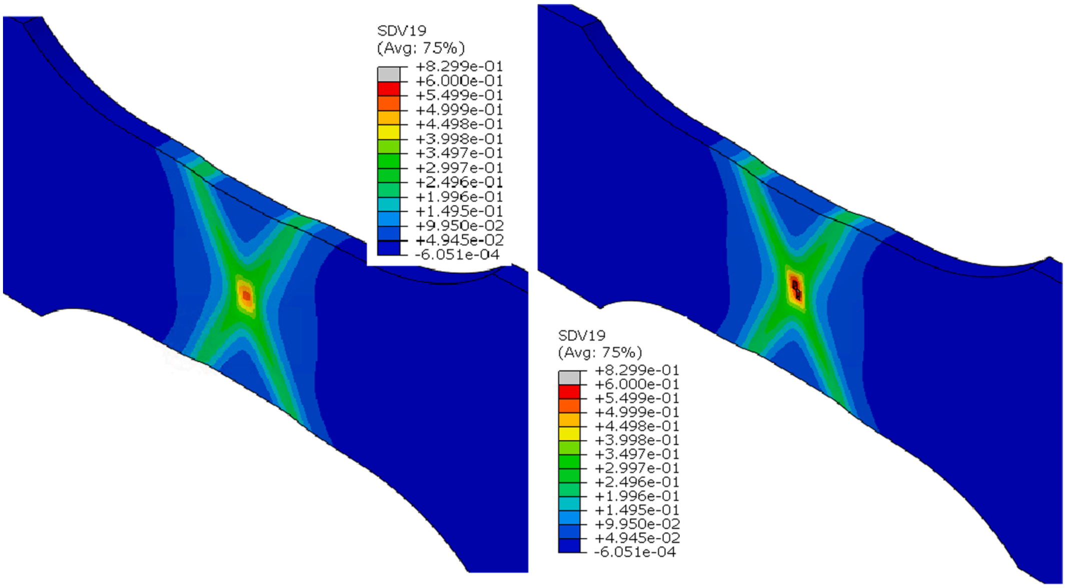

(a) d=10.6mm (b) d=10.8mm

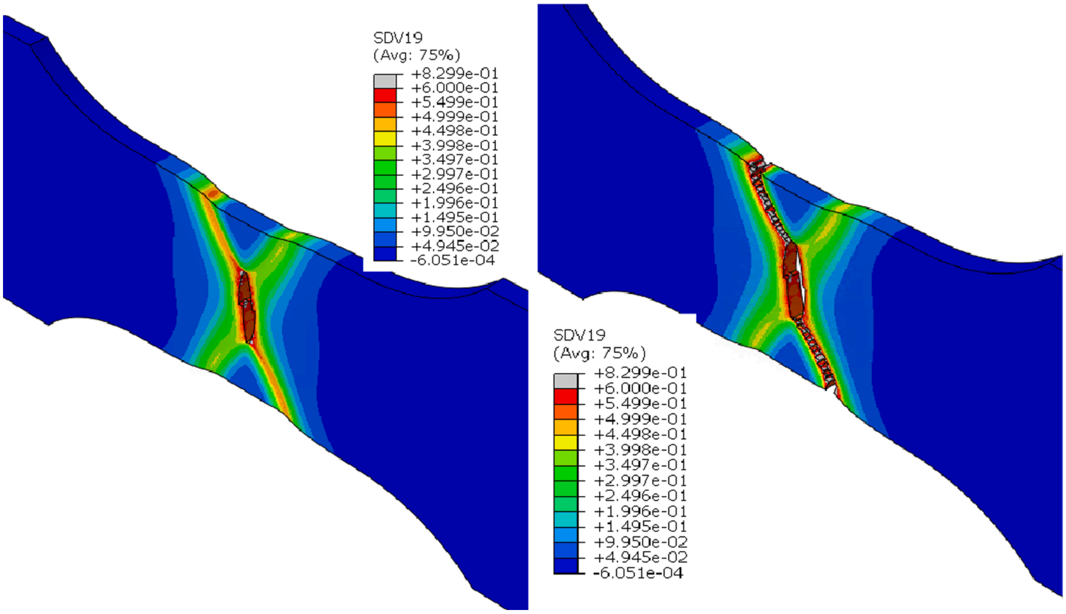

(b) d=14.9mm (b) d=16.5mm

Fig. 20. Failure Process and equivalent plastic strain distribution of S960(A)/0 (SDV19: Equivalent plastic strain).

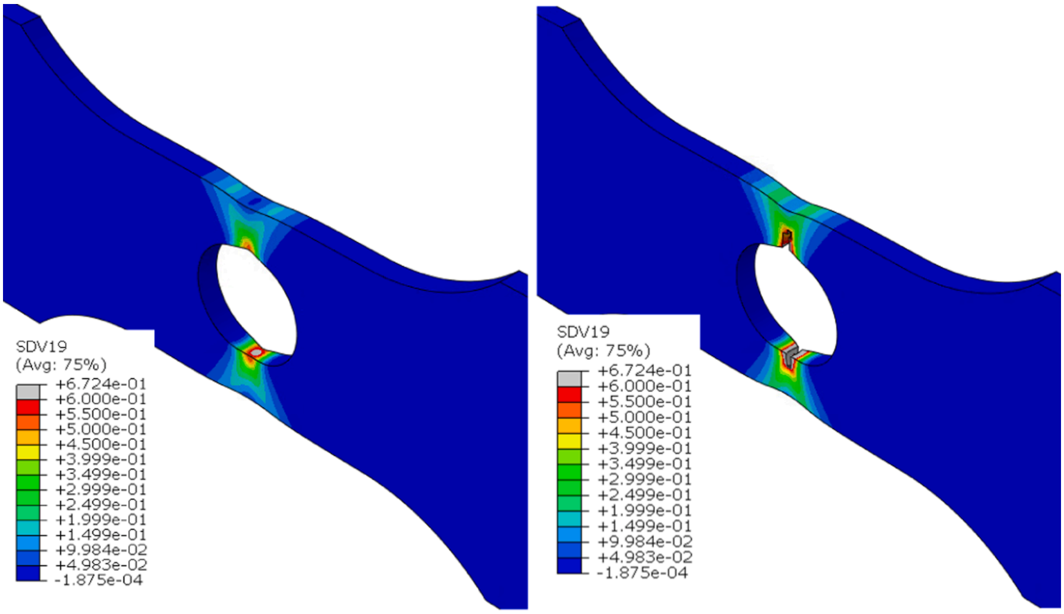

(a) d=4.3mm (b) d=5.6mm

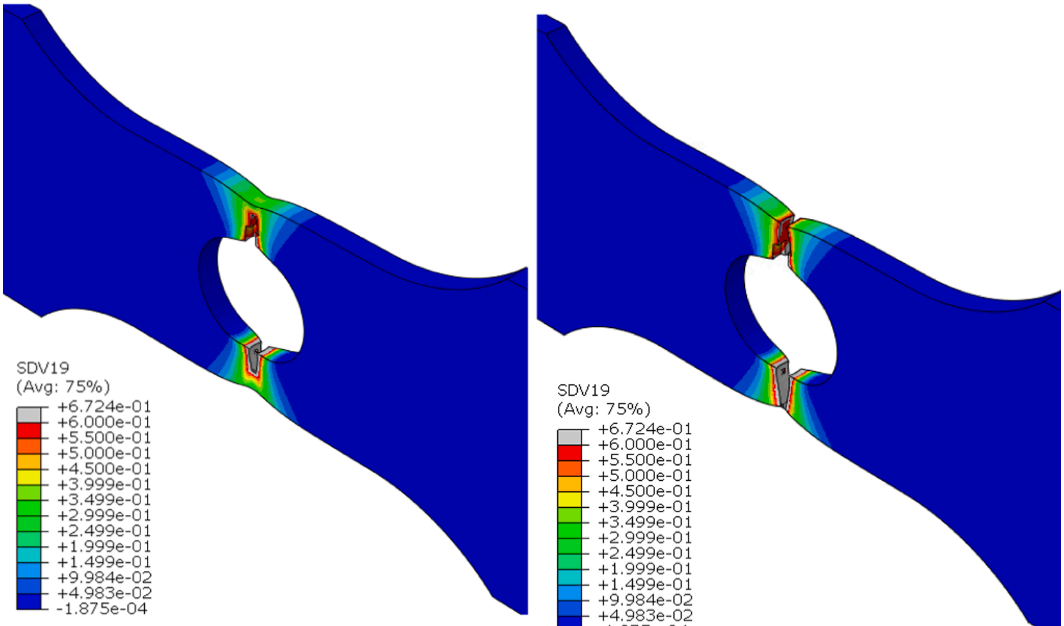

(c) d=6.9mm

(d) d=9.0mm

Fig. 21. Failure Process and equivalent plastic strain distribution of S700(A)/40(SDV19: Equivalent plastic strain).

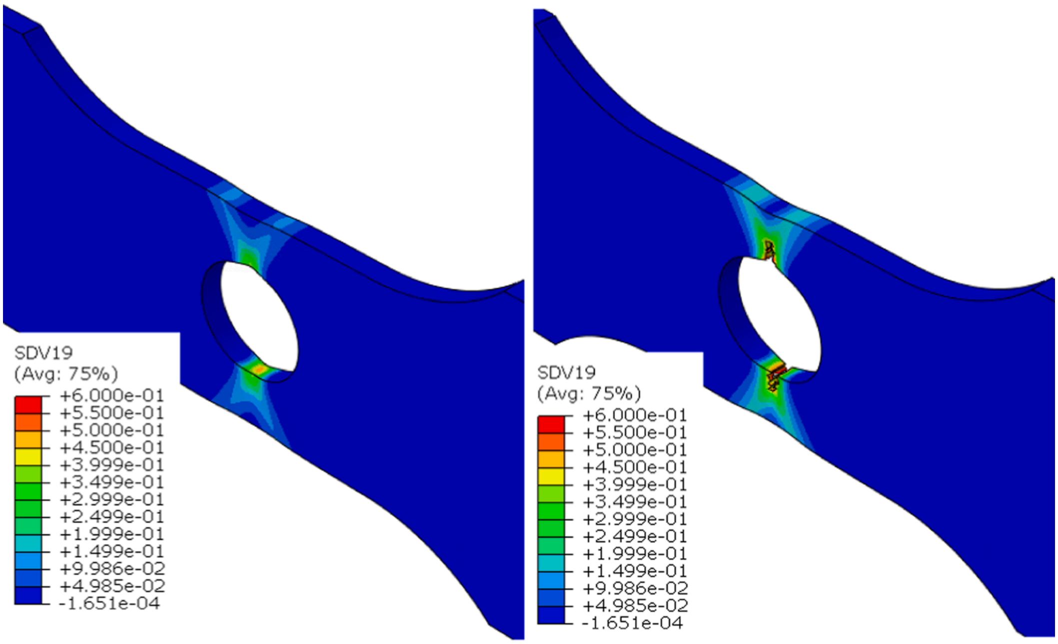

(a) d=3.0mm (b) d=4.5mm

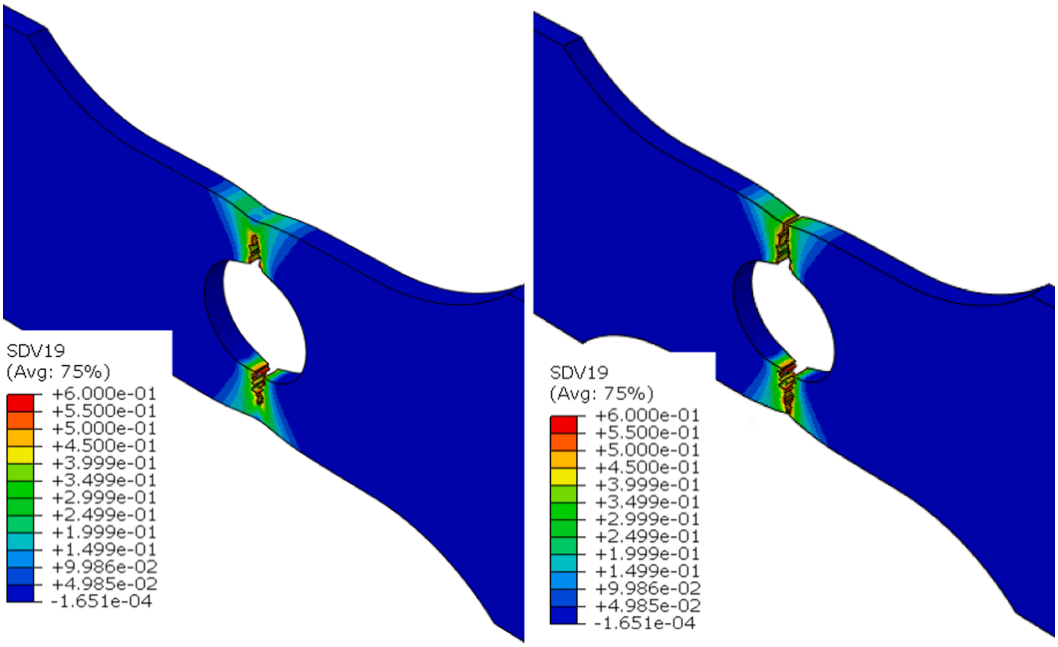

(c) d=5.8mm (d) d=7.2mm

Fig. 22. Failure Process and equivalent plastic strain distribution of S960(A)/40 (SDV19: Equivalent plastic strain).

Table 8
Steel grades used in the case study.

	f_y [MPa]	f_u [MPa]	ε_A [\%]]	f_u/f_y
S700(A)	753	842.0	17.0	1.12
S700(B)	751	830.1	11.9	1.11
S960(A)	1018	1052.0	11.9	1.03
S960(B)	1060	1181.3	9.17	1.11

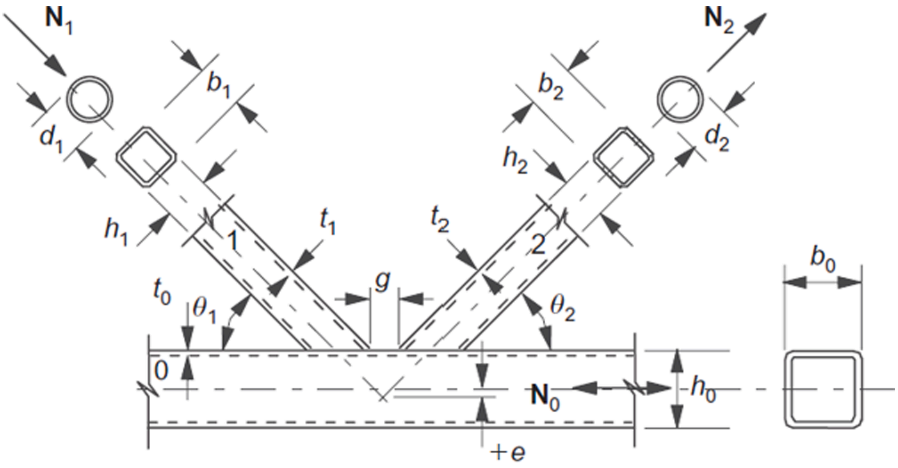

Fig. 23. K gap joint parameters.

Table 9
Joint geometry for the parametric study.

b_o (mm)	t_o (mm)	b_i (mm)	t_i (mm)	g (mm)	θ_i (°)	e (mm)	β (–)
140	6.3	70	5	40	30	−18	0.50

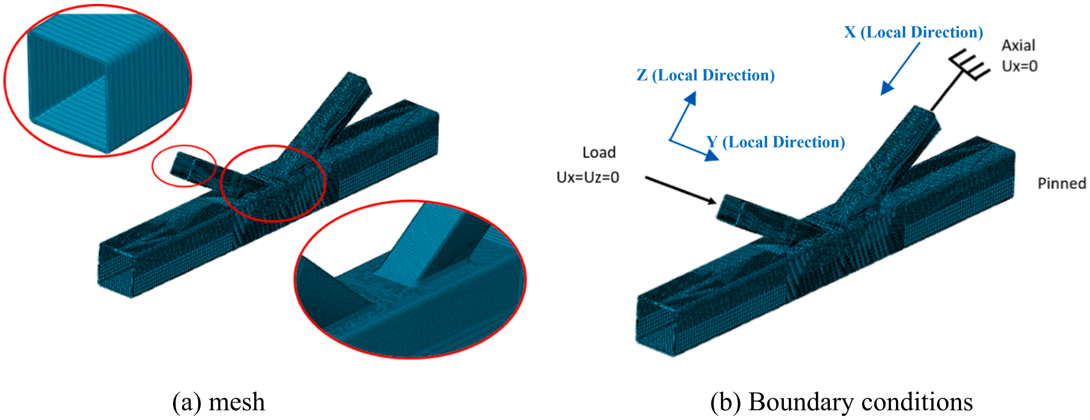

(a) mesh (b) Boundary conditions

Fig. 24. Finite element mesh and boundary conditions of the K gap joint.

fracture strain of S700(B) compare to the fracture strain of S700(A) is shown both on joint resistance up to 5% depending on the material model used, and on the deformation capacity up to 45% difference between the models, see Fig. 25.b. It is interesting to note that the maximum resistance is obtained using the EPHD material model, but not for EPH material model, which would be expected base on the material assumption, as it was the case for S700(A) material.

The load-deformation relationship of K gap joints made of S960 is shown in Fig. 26. The characteristic resistance is 853.8kN using material factor $C_f = 0.8$ acc. to [35]. The force at 3% deformation is governing and the values are 1131.8kN, 1155.6kN, and 1142.7kN for the joint assuming material properties S960(A)-EPH, S960(A)-EPHD, and S960(A)-EPHDF, respectively. The characteristic resistance, which is the same as the characteristic resistance acc. to [35] is 0.75, 0.74 and 0.75 at 3% deformation for the joint using material properties S960(A)-EPH, S960(A)-EPHD, and S960(A)-EPHDF, respectively. The force at 3% deformation or maximum force is 1201.2kN, 1263.8 kN, 1240.9kN for the joint using material properties S960(B)-EPH, S960(B)-EPHD, and S960(B)-EPHDF respectively. The characteristic resistance is 071, 0.69 and 0.68 at 3% deformation for the joint using material properties S960(B)-

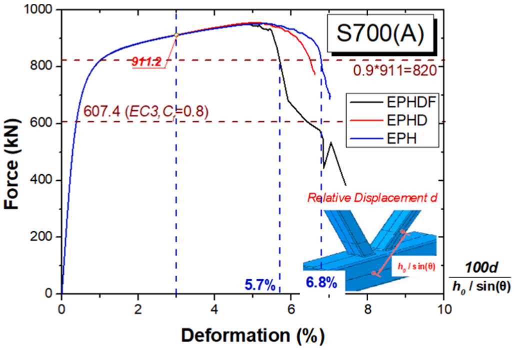

(a) S700A

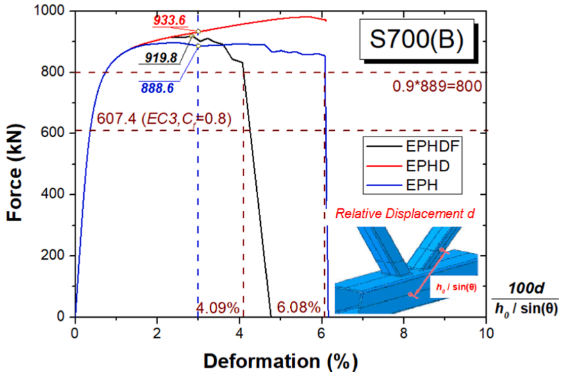

(b) S700B

Fig. 25. Load-deformation relationship of hollow section joints made of S700.

EPH, S960(B)-EPHD, and S960(B)-EPHDF respectively.

For the steel grade, S960(B) which has significantly smaller engineering fracture strain compare to S960(A), 9.2% vs 12%, respectively, leading to larger differences in the force at 3% deformation, up to 5% than in case of a more ductile material. The same pattern of behavior in relation to the joint resistance depending on the material model used is observed in the analysis of S960 steels. These findings underline needs to use EPHDF model to achieve a reliable prediction of the maximum force and the deformation capacity.

The failure modes of K gap joints using material properties EPH, EPHD, and EPHDF of S700(B) and S960(A), respectively are shown in Fig. 27 and Fig. 28. The chord face failure, due to a relatively smaller $\beta = 0.5$, is obtained when using material properties EPHDF in Fig. 27(c) and Fig. 28(c). For the same joints using material properties EPH in Fig. 27(a) and Fig. 28(a), the maximum equivalent plastic strain is redistributed to the brace due to “fake” local support ensured from chord face. For the same joints using material properties EPHD in Fig. 27(b) and Fig. 28(b), local buckling occurred near the brace due to “fake” local support ensured from chord face. The above mention finding underlines the requirement to use the EPHDF model in order to achieve a reliable failure mode.

The crack propagation process of the joint made of S700(B) and S960(A), respectively is shown in Fig. 29. The crack initiates around the weld toe of the tensile brace at 4.25% and 4.35% of the relative displacement for S700(B) and S960(A), respectively. Thereafter, the fracture occurs near the side and back weld toe of the compressive brace when the relative displacement reached to 6.50% and 6.00% of the relative displacement for S700(B) and S960(A), and the final fracture occurs between the compressive and tensile brace when the relative displacement reaches to 7.50% and 8.75% of the relative displacement for S700(B) and S960(A) respectively.

The failure modes indicate an inconsistency between the position of the maximum equivalent plastic strain at the maximum force and the fracture position if the fracture is not considered. The local buckling of the brace appears in the case of EPH material caused by the “fake stiffness” of the chord face. Another interesting observation is that the most optimistic prediction is obtained for EPLHD material model in which elements with excessively high strains and lower resistance of elements in the chord face are not deleted from the chord face but providing the “fake stiffness” and the “fake resistance” of the joint. The above-mentioned observations indicate that the only reliable approach would be a material model based on EPHDF model.

The aforementioned observation most probably will not be observed in the physical experiment, because of the simplification of the FE model used here. However, the possible scattering from the physical experiment does not influence the main motivation for the use

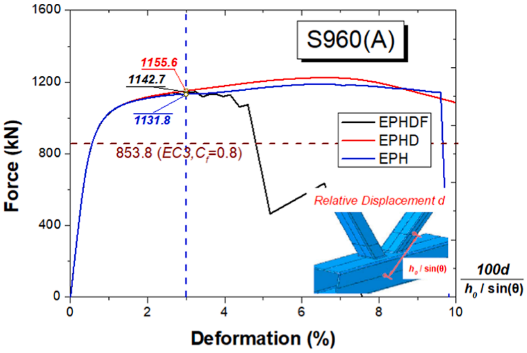

(a) S960(A)

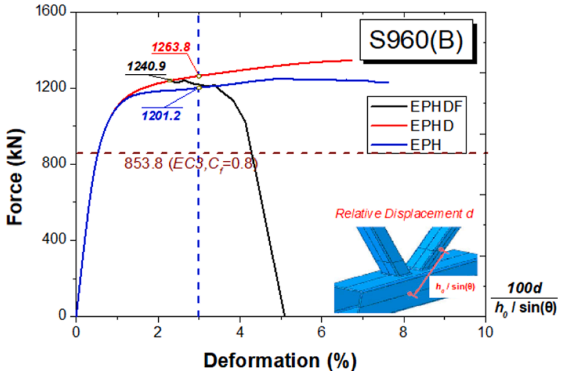

(b) S960(B)

Fig. 26. Load-deformation relationship of hollow section joints made of S960.

of EPHDF model. Obviously, more research data would be needed to experimentally establish fracture properties of HAZ and filler material.

6. Conclusions and future study

One of the challenging issues of HSS used in the construction sector is how to identify the parameters of the phenomenological ductile fracture model. The current method is mainly based on a series of material tests with different stress status achieved through different initial specimen geometries or by applying different load combinations. An attempt is made to evaluate the ductile fracture of HSS only from the uniaxial stress-strain curve in this paper. Following conclusions could be drawn:

(1) Uncoupled fracture model was implemented through a user subroutine VUMAT (ABAQUS) to evaluate the ductile fracture of HSS, where a rate-independent non-linear isotropic J2 hardening model is used in conjunction with a separate Hosford-Coulomb fracture model.

(2) A detailed procedure to identify the material parameters based on only the uniaxial stress-strain curve of HSS is proposed. This paper divides the whole uniaxial stress-strain relationship of HSS into three stages: elastic stage, plastic stage, and coupled plastic-damage stage. The coupled plastic-damage stage is further decomposed into the plastic-dominated zone and the damage-dominated zone. The parameters are calibrated in terms of different stages. The fracture strain at multiaxial loading status is proposed to be a proportional rescaling of the equivalent plastic strain when the true stress reaches the top. The fracture parameters are obtained by computational homogenization and a rescaling parameter. The identified parameters are successfully validated based on the experimental results of the HSS plate with different hole sizes in the middle. The root mean error (RME) by comparing the force at the same displacement in the softening stage between experiments and FE is around 10% and 15% for steel from producer A and B, respectively.

(3) Ductile fracture of an individual K gap joint made of square hollow sections was simulated as a case study. The ductile behavior and resistance of K gap joints are better than the recommendations from European standard part 1–8-chapter 9 due to a relatively smaller $\beta = 0.5$. The characteristic resistance with a 0.8 material factor (C_f) is 0.67 and 0.66 FE results for K gap joints made of S700(A) and S700(B), and is 0.75 and 0.68 of FE results for K gap joints made of S960(A) and S960(B) respectively. All

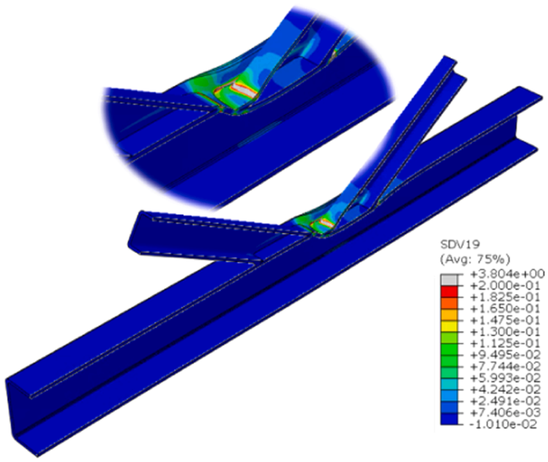

(a) S700(B)-EPH

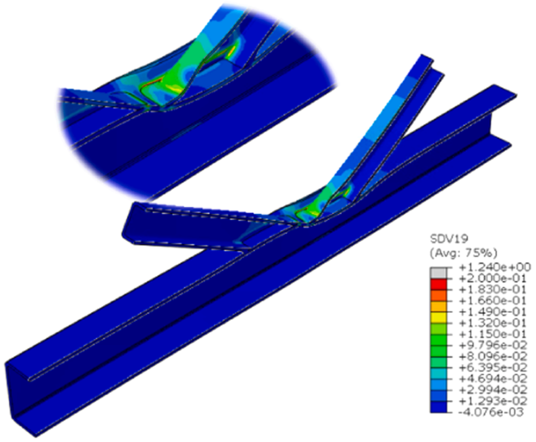

(b) S700(B)-EPHD

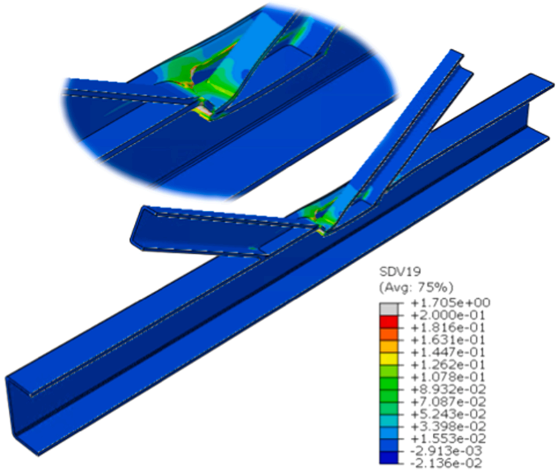

(c) S700(B)-EPHDF

Fig. 27. Failure mode of K gap joint made of S700(B) (SDV19: Equivalent plastic strain).

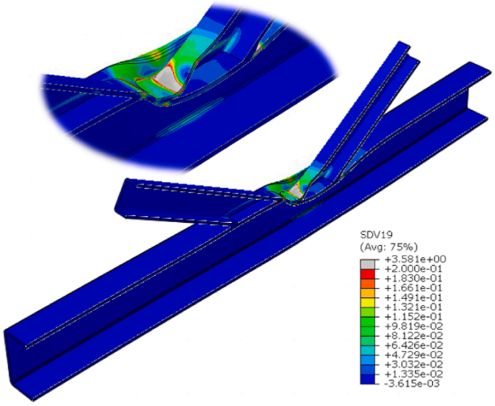

(a) S960 (A)-EPH

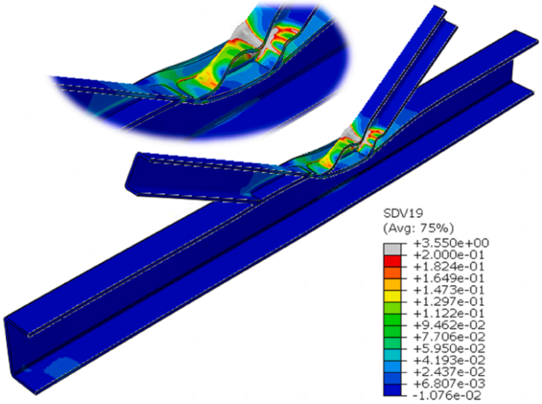

(b) S960 (A)-EPHD

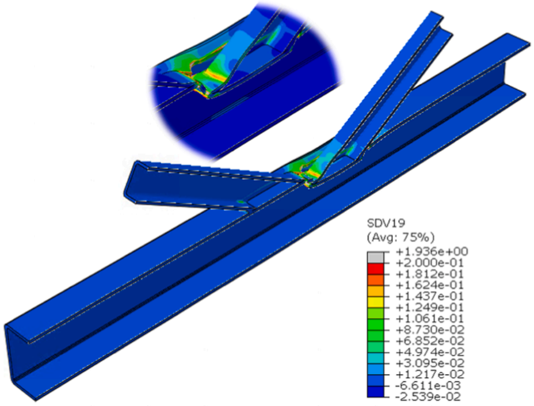

(c) S960 (A)-EPHDF

Fig. 28. Failure mode of K gap joint made of S960(A) (SDV19: Equivalent plastic strain).

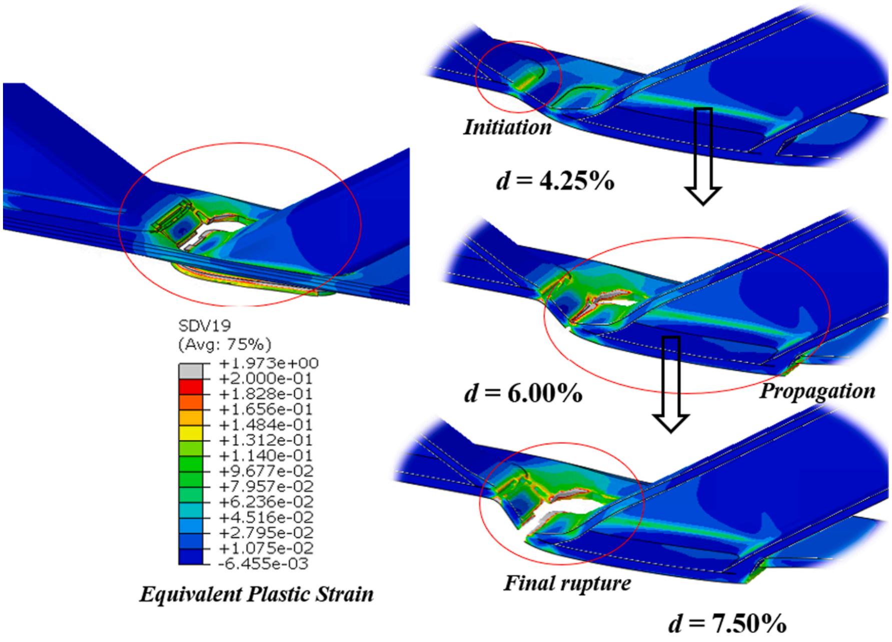

(a) S700 (B)

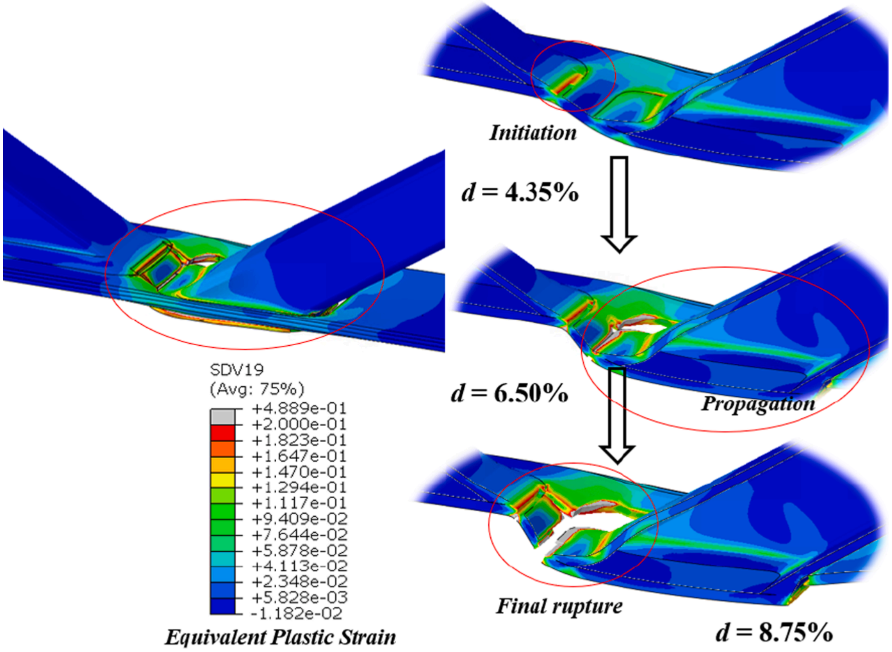

(b) S960 (A)

Fig. 29. Crack propagation of the K gap joint (SDV19: Equivalent plastic strain).

the K gap joints present chord face failure due to $\beta = 0.5$. The crack initiated is around the weld toe of tensile brace, after then, the fracture occurred near the side and back weld tone of the compressive brace, and the final fracture occurred between the tensile and compressive brace.

(4) Further research is needed to improve the prediction accuracy: (i) Identification of the ductile fracture parameters based on the unit cell with physical meaning, such as a microvoid in the middle. (ii) The mesh size is fixed as 1 mm in this paper. The non-local approach is expected in the future to alleviate the mesh size effects. (iii) The simulation results are needed further validated by shear-dominated fracture specimens.

Declaration of Competing Interest

The authors declare that they have no known competing financial interests or personal relationships that could have appeared to influence the work reported in this paper.

References

[1] X.-L. Zhao, Section capacity of very high strength (VHS) circular tubes under compression, Thin-Walled Struct. 37 (3) (2000) 223–240.
[2] R. Bjorhovde, Development and use of high performance steel, J. Constr. Steel Res. 60 (3-5) (2004) 393–400.
[3] M. Veljkovic, B. Johansson, Design of hybrid steel girders, J. Constr. Steel Res. 60 (3-5) (2004) 535–547.
[4] H. Xin, A.F.O. Correia José, M. Veljkovic, Three-dimensional Fatigue Crack Propagation Simulation Using Extended Finite Element Methods for Steel Grades S355 and S690 Considering Mean Stress Effects, Eng. Struct. https://doi.org/10.1016/j.engstruct.2020.111414.
[5] H. Xin, M. Veljkovic, Fatigue crack initiation prediction using phantom nodes-based extended finite element method for S355 and S690 steel grades, Eng. Fract. Mech. 214 (2019) 164–176.
[6] H. Xin, M. Veljkovic, Residual stress effects on fatigue crack growth rate of mild steel S355 exposed to air and seawater environments, Mater. Des. 193 (2020) 108732, https://doi.org/10.1016/j.matdes.2020.108732.
[7] A.A. Benzerga, J.-B. Leblond, Ductile fracture by void growth to coalescence, in: Advances in Applied Mechanics. Adv Appl Mech 10 (2010) 169–305. https://doi.org/10.1016/S0065-2156(10)44003-X.
[8] F.A. McClintock, A criterion for ductile fracture by the growth of holes, 1968.
[9] J.R. Rice, D.M. Tracey, On the ductile enlargement of voids in triaxial stress fields*, J. Mech. Phys. Solids 17 (3) (1969) 201–217.
[10] A.L. Gurson, Continuum theory of ductile rupture by void nucleation and growth: Part I—Yield criteria and flow rules for porous ductile media, 1977.
[11] V. Tvergaard, Influence of voids on shear band instabilities under plane strain conditions, Int. J. Fract. 17 (4) (1981) 389–407.
[12] V. Tvergaard, A. Needleman, Analysis of the cup-cone fracture in a round tensile bar, Acta Metall. 32 (1) (1984) 157–169.
[13] A.A. Benzerga, J. Besson, Plastic potentials for anisotropic porous solids, Eur. J. Mech. A. Solids 20 (3) (2001) 397–434.
[14] K. Nahshon, J.W. Hutchinson, Modification of the Gurson Model for shear failure, Eur. J. Mech. A. Solids 27 (1) (2008) 1–17.
[15] G.R. Johnson, W.H. Cook, A constitutive model and data for metals subjected to large strains, high strain rates and high temperatures, Proc. 7th Int. Symp. Ballist., vol. 21, The Netherlands, 1983, p. 541–547.
[16] Y. Bai, T. Wierzbicki, Application of extended Mohr–Coulomb criterion to ductile fracture, Int. J. Fract. 161 (1) (2010) 1–20.
[17] C.C. Roth, D. Mohr, Ductile fracture experiments with locally proportional loading histories, Int. J. Plast. 79 (2016) 328–354.
[18] M. Dunand, D. Mohr, Hybrid experimental–numerical analysis of basic ductile fracture experiments for sheet metals, Int. J. Solids Struct. 47 (9) (2010) 1130–1143.
[19] D. Mohr, S.J. Marcadet, Micromechanically-motivated phenomenological Hosford–Coulomb model for predicting ductile fracture initiation at low stress triaxialities, Int. J. Solids Struct. 67-68 (2015) 40–55.
[20] Y. Bai, T. Wierzbicki, A new model of metal plasticity and fracture with pressure and Lode dependence, Int. J. Plast. 24 (6) (2008) 1071–1096.
[21] Y. Bao, T. Wierzbicki, On fracture locus in the equivalent strain and stress triaxiality space, Int. J. Mech. Sci. 46 (1) (2004) 81–98.
[22] Y. Lou, J.W. Yoon, H. Huh, Modeling of shear ductile fracture considering a changeable cut-off value for stress triaxiality, Int. J. Plast. 54 (2014) 56–80.
[23] T.S. Cao, Models for ductile damage and fracture prediction in cold bulk metal forming processes: a review, Int. J. Mater. Form 10 (2) (2017) 139–171.
[24] L.H. Pál Turána, Experimental behaviour of tension plates with centre hole made from high strength steel. Nord. Steel Constr. Conf. 2015, Tampere, Finland, 2015.
[25] Rui Yan, Haohui Xin, Milan Veljkovic, Identification of GTN damage parameters as a surrogate model for S355, Proc. 17th Int. Symp. Tubul. Struct., Singapore, 2019. https://doi.org/10.3850/978-981-11-0745-0_066-cd.
[26] H. Xin, S. Sun, J. Fish, A surrogate modeling approach for additive-manufactured materials, Int. J. Multiscale Comput. Eng. (2017).
[27] H. Xin, WaiChing Sun, J. Fish, Discrete element simulations of powder-bed sintering-based additive manufacturing, Int. J. Mech. Sci. 149 (2018) 373–392.
[28] V. Abaqus, 6.14 Documentation, Dassault Syst Simulia Corp (2014).
[29] F.D. Fischer, O. Kolednik, G.X. Shan, F.G. Rammerstorfer, A note on calibration of ductile failure damage indicators, Int. J. Fract. 73 (4) (1995) 345–357.
[30] W. Ramberg, W.R. Osgood, Description of stress-strain curves by three parameters, 1943.
[31] Y. Ling, Uniaxial true stress-strain after necking, AMP J. Technol. 5 (1996) 37–48.
[32] H. Xin, A. Mosallam, Y. Liu, M. Veljkovic, J. He, Mechanical characterization of a unidirectional pultruded composite lamina using micromechanics and numerical homogenization, Constr. Build. Mater. 216 (2019) 101–118.
[33] H. Xin, M. Nijgh, M. Veljkovic, Computational homogenization simulation on steel reinforced polymer used in the injected bolted connections, Compos. Struct. 210 (2019) 942–957.
[34] 1993-1-1 EN. Eurocode 3: Design of steel structures: General rules and rules for buildings, 2005.
[35] Standardization. EN1993-1-8 ver. 2020-03-30. Eurocode 3: Design of steel structures - Part 1-8: Design of joints. n.d.